

# XFEM Modeling of Short Microfiber Reinforced Composites with Cohesive Interfaces

Matthew G. Pike\* and Caglar Oskay†

Department of Civil and Environmental Engineering  
Vanderbilt University  
Nashville, TN 37235

## Abstract

This manuscript presents the formulation and implementation of a failure model for random short microfiber reinforced composite materials based on the Extended Finite Element Method (XFEM). Elastic and deformable microfiber inclusions modeled as objects with zero measure are incorporated into the XFEM framework. A new debonding enrichment function is proposed to idealize the progressive debonding between the fiber-matrix interfaces. The proposed manuscript provides a modeling strategy particularly suitable for very high aspect ratio inclusions. The fiber deformation is approximated as axial and directly incorporated into the Lagrangian. The progressive failure within the matrix material is idealized using an integral-type nonlocal damage model. The performance of the proposed XFEM model is assessed by comparing model predictions to the direct finite element method for various fiber configurations. The numerical verification studies point to high accuracy characteristics of the proposed approach. The computational efficiency of the approach provides the capability to evaluate the failure response of microstructures that include a large number of short fiber inclusions.

*Keywords:* Random short fibers, extended finite element, cohesive zone law, fiber reinforced composites

---

\*Author address: VU Station B#351831, 2301 Vanderbilt Place, Nashville, TN 37235. Email: matthew.g.pike@vanderbilt.edu

†Corresponding author address: VU Station B#351831, 2301 Vanderbilt Place, Nashville, TN 37235. Email: caglar.oskay@vanderbilt.edu

# 1 Introduction

Microfibers introduced into a cementitious material can significantly alter and improve the mechanical properties, such as the elastic modulus, load carrying capacity, flexural strength and flexural toughness [1, 2]. In addition to the mechanical properties, the fiber reinforcements also provide unique functional properties that include self sensing, self control of cracks and electromagnetic field shielding, and others [3, 4, 5, 6, 7].

Microfiber reinforced composite material modeling to extract elastic and inelastic homogenized properties, are traditionally conducted based on micromechanical modeling or through computational studies of representative volume elements (RVEs). The micromechanical modeling approaches are usually based on the Eshelby's solution of ellipsoidal inclusions embedded in a matrix in conjunction with Mori-Tanaka scheme (e.g., [8, 9, 10]), Hashin-Strichman bounds [11] and others. To mimic the effect of the fiber geometries when such approaches are applied to model random fibers, the ellipsoidal inclusions are assumed to have high aspect ratios. Direct RVE modeling of fiberous composites, where the fibers are resolved, have also been proposed (e.g. [12, 13, 14]). The 3-D resolution of the randomly generated fiber geometries is challenging when the fiber aspect ratios are large due to the requirement of fiber domain discretization with small elements, and to ensure mesh compatibility between the embedded fibers and the matrix when large number of fibers are present.

The fundamental purpose of employing the extended finite element method (XFEM) is to eliminate the need to discretize the individual fibers and compatibility of the underlying discretization. The primary idea of the XFEM approach is to enrich the standard finite element basis with nodal enrichment functions capable of representing inhomogeneities and discontinuities within the problem domain without explicitly representing them through meshing [15, 16]. The partition of unity principle [17] is employed to retain the local character of the base finite element formulation as well as in the recovery of the original form of the enrichment function, which accurately represents the local behavior. The discontinuities modeled by XFEM may be strong (i.e., displacement discontinuities [18]), suited to model cracks or weak (i.e., strain discontinuities [19]) to model internal boundaries such as inclusions.

While the XFEM approach can be used to model the cracks and inclusions (e.g. [20, 21, 22, 23, 24]), it does not readily account for the progressive debonding along the inclusion interfaces. Cohesive zone modeling, which requires the resolution of the interfaces, has been the traditional approach to idealize progressive debonding. Cohesive zone modeling describes the material separation between two surfaces by incorporating zero thickness elements between solid elements that discretize the neighboring domains and relating tractions at the surface of the interface to displacement jumps through softening a constitutive equation (i.e., a cohesive law). Cohesive zone modeling applied to fiber reinforced composites are available for pure

mode and mixed mode cohesive laws in [25, 26, 27, 28, 29, 30, 31], among many others.

Cohesive zone modeling has recently been incorporated into the XFEM framework. Moës and Belytschko [32] and Unger et al. [33] have proposed methods to model cohesive crack growth in concrete. Zi and Belytschko [34] presented a formulation of crack tip elements for cohesive cracks. Work on partly cracked XFEM elements with cohesive cracks was performed by Asfreg et al. [35]. Bouhala et al. [36] focused on the interfacial debonding of cracks for long fiber reinforced composites. Other applications include the regularization of the discontinuity at cohesive interfaces for modeling delamination in composites [37] and in the context of a multiscale framework for composites combining XFEM with cohesive zone laws [38].

The enrichment idea to eliminate the need to discretize individual fibers have been proposed by Radtke and co-workers [39, 40]. They were first to employ the partition of unity method with fibers as zero measure elastic inclusions for idealizing fiber reinforced composite behavior. A Heaviside enrichment function was used to account for the strong discontinuity present due to tangential debonding at the fiber-matrix interface. The weak discontinuity in the response field due to the presence of the fiber was not included in the response field approximation. A non-linear cohesive law was employed to describe tangential slip along the fiber-matrix interface and the normal fiber-matrix interface separation was suppressed.

In this manuscript, we present the formulation and implementation of a progressive failure model for random short microfiber reinforced composite materials. In a 2-D setting, fiber inclusions are modeled as elastic objects of zero measure using the XFEM approach. The presence of elastic inclusions and the progressive normal and tangential debonding of the fiber from the matrix are modeled through inclusion and debonding enrichment functions. By this approach, the need to resolve inclusions using solid or structural elements and the debonding process using cohesive elements are eliminated. With extension to 3-D in mind, the progressive cracking in the matrix is idealized using an integral-type nonlocal continuum damage mechanics model. Numerical integration procedures are provided for accurate evaluation of the system response for fibers at random positions within the problem domain. The performance of the proposed XFEM model is assessed against the direct finite element method for various fiber configurations. While the general methodology of representing the fibers as zero measure follows the principles of ideas presented in Refs. [39, 40], the current manuscript introduces the following novel contributions: (1) A new debonding enrichment function is proposed to incorporate cohesive traction-separation behavior between the fiber inclusions and the matrix; (2) The present formulation accounts for decohesion in both tangential and normal directions; and (3) The weak discontinuity (strain discontinuity) across the fiber domain is incorporated through XFEM enrichment.

The remainder of this manuscript is organized as follows. In Section 2, the enrichment functions employed to model the presence of the inclusions and the debonding process are

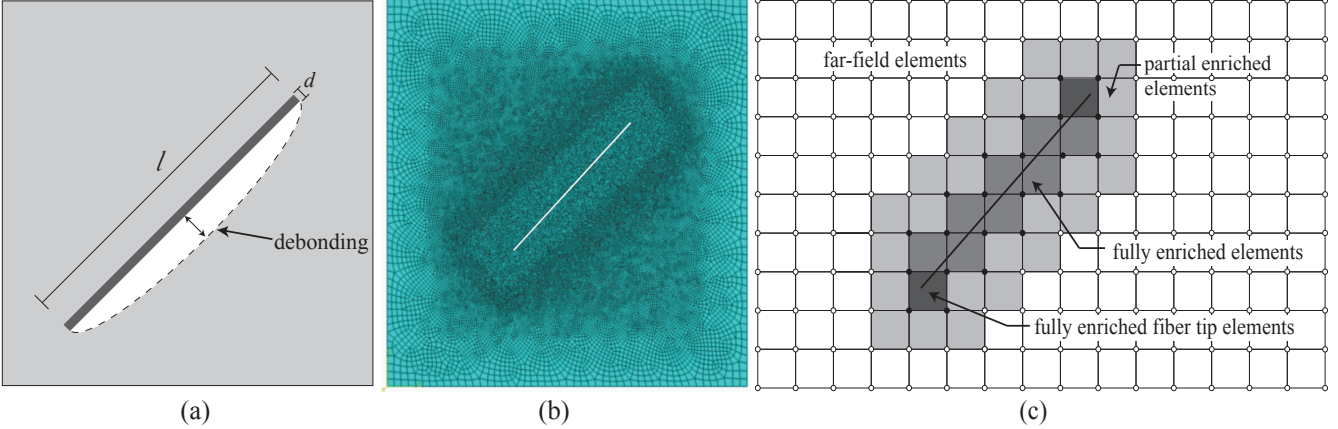


Figure 1: (a) Fiber representation in the domain with the white area representing the debonding between the fiber and the matrix; (b) standard finite element mesh for a short fiber inclusion composite; and (c) the decomposition of the problem domain into subdomains of far-field elements approximated by standard basis, partially enriched elements, and fully enriched elements.

introduced. Section 3 provides the governing equations and the model formulation. The computational formulation is discussed in Section 4, including the formulation of fiber deformation, formulation of cohesive tractions, numerical integration and the treatment of partially enriched elements. Numerical verification studies to assess the performance of the proposed approach are presented in Section 5. Conclusions and future research directions in this area are discussed in Section 6.

## 2 XFEM for Short Fiber Reinforced Composites

We seek to model short fiber reinforced composites with very high aspect ratios ( $d/l \ll 1$ ), as illustrated in Fig. 1a. The high aspect ratio of fibers renders the resolution of the fiber geometry infeasible within the finite element method (Fig. 1b), particularly when a large number of fibers is present. In this manuscript, the extended finite method (XFEM) is employed to eliminate the need to conform the discretization to the individual fibers (Fig. 1c). The XFEM is employed not only to describe the presence of the fiber inclusions, but also to idealize the fiber-matrix debonding process.

XFEM utilizes enrichment functions to model the presence of inclusions and discontinuities in an otherwise uniform domain. The foundation for how to incorporate of the enrichment function into the finite element framework is the partition of unity method (PUM), formalized by Babuska and Melenk [17]. In PUM, the nodal level enrichment is a product of the enrichment function and the standard shape functions that satisfy the partition of unity property for the enrichment, in addition to the standard basis. The enrichment functions are known a-priori to represent the response well within the whole domain or a subdomain of the problem,

around strong or weak discontinuities.

We consider the following discretization of the displacement field for a domain reinforced by short fiber inclusions:

$$\mathbf{u}(\mathbf{x}) = \sum_{a=1}^{n_n} N_a(\mathbf{x}) \hat{\mathbf{u}}_a + \sum_{b=1}^{n_{\text{en}}} N_{\mathcal{I}_b}(\mathbf{x}) \psi(\mathbf{x}) \hat{\mathbf{c}}_b + \sum_{c=1}^{n_{\text{en}}} N_{\mathcal{I}_c}(\mathbf{x}) \Upsilon(\mathbf{x}) \hat{\mathbf{d}}_c \quad (1)$$

in which,  $\mathbf{u}$  denotes the displacement fields;  $N_a$ , the standard finite element shape function associated with node  $a$ ;  $\hat{\mathbf{u}}_a$ ,  $\hat{\mathbf{c}}_b$  and  $\hat{\mathbf{d}}_c$  the nodal coefficients of the standard, fiber enrichment and debonding enrichments, respectively;  $n_n$  the total number of mesh nodes in the finite element discretization;  $n_{\text{en}}$  the number of enriched nodes;  $\mathcal{I}$  index set of enriched nodes;  $\mathcal{I}_a \in \mathcal{I}$  the index of an enriched node,  $a$ ;  $\psi$  the fiber enrichment function; and  $\Upsilon$  denotes the debonding enrichment function.

In Eq. 1, the first right hand side term corresponds to the standard finite element approximation of the response field. The enrichment,  $\psi$ , that accounts for the presence of the fiber within the domain, represents the strain discontinuity in the approximation space. The third term on the right hand side is the enrichment to approximate the displacement jump due to the progressive loss of the cohesive bond between the fiber and the matrix, and is a function of the debonding enrichment function,  $\Upsilon$ .

## 2.1 Fiber enrichment function

The enrichment function for the high aspect ratio short fiber inclusions was previously developed by the authors [41] and the function is described below for completeness. The fiber enrichment function is expressed in terms of level set functions for the domain and the tips of the fiber. For simplicity of the presentation, we consider a single inclusion to present the enrichment function. In the case when multiple fibers are present, each fiber is represented by a separate enrichment function. The generalization to the case of multiple fibers is straightforward provided that multiple enrichments are not present within the same finite element. We note that presence of multiple enrichment functions in a single finite element does not refer to the overlapping of the fiber domains, the latter being nonphysical. In this study, the presence of multiple enrichment functions in a single finite element due to separate fibers is not investigated.

To model the level set functions, we consider the open bounded domain of the composite body,  $\Omega \subset \mathbb{R}^2$ . The reinforcing fiber is entirely embedded in  $\Omega$ . The fiber is taken to have a high aspect ratio and to be straight. The domain of the fiber is therefore approximated as a line segment, parameterized by  $s$ , such that:

$$\mathbf{x} = \mathbf{x}_c + \frac{\mathbf{x}_2 - \mathbf{x}_1}{2} s; \quad -1 \leq s \leq 1; \quad \mathbf{x} \in \Gamma \quad (2)$$

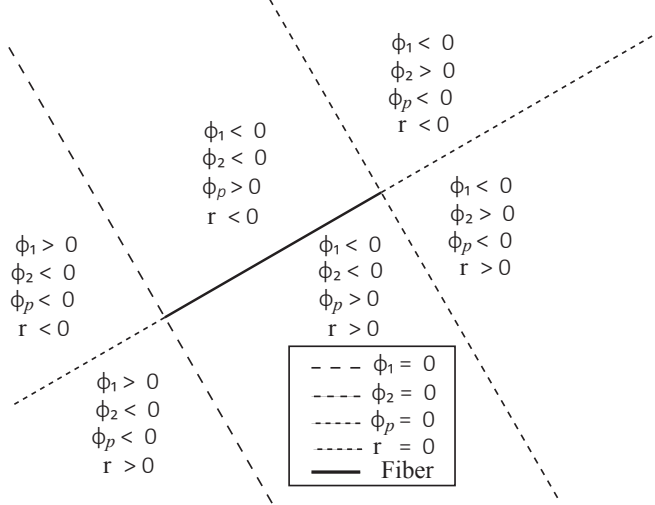


Figure 2: Functions of the fiber enrichment and debonding enrichment.

where,  $\mathbf{x}_1$  and  $\mathbf{x}_2$  and  $\mathbf{x}_c$ , are the positions of the fiber tips and the position of the center of the fiber (i.e.,  $\mathbf{x}_c = (\mathbf{x}_1 + \mathbf{x}_2)/2$ ), respectively. The fiber tip level set functions are expressed as:

$$\phi_\alpha(\mathbf{x}) = (\mathbf{x} - \mathbf{x}_\alpha) \cdot \mathbf{t}_\alpha; \quad \alpha = 1, 2 \quad (3)$$

where,  $\mathbf{t}_\alpha$  denotes the tangent at the fiber tip,  $\alpha$  (i.e.,  $\mathbf{t}_1 = (\mathbf{x}_1 - \mathbf{x}_2)/l$  and  $\mathbf{t}_2 = (\mathbf{x}_2 - \mathbf{x}_1)/l = -\mathbf{t}_1$ ); and  $l = \|\mathbf{x}_2 - \mathbf{x}_1\|$  is the length of the fiber.  $\phi_\alpha$  provides the zero level set along the plane normal to the fiber passing through the fiber tip.  $\phi_\alpha$  is positive on the outer part of the domain cut by the zero level set, and negative elsewhere within the composite body (Fig. 2).

The level set associated with the domain of the fiber,  $\phi_c(\mathbf{x})$ , divides the domain of the body along the plane of the fiber with positive values on each side and has zero value along the fiber.

$$\phi_c(\mathbf{x}) = \|\mathbf{x} - \mathcal{P}(\mathbf{x})\| \quad (4)$$

in which,  $\mathcal{P}(\mathbf{x})$  is the projection of  $\mathbf{x}$  onto the fiber:

$$\mathcal{P}(\mathbf{x}) = \mathbf{x}_1 + [(\mathbf{x} - \mathbf{x}_1) \cdot \mathbf{t}_2] \mathbf{t}_2 = \mathbf{x}_2 + [(\mathbf{x} - \mathbf{x}_2) \cdot \mathbf{t}_1] \mathbf{t}_1 \quad (5)$$

Using the level set function from Eqs. 3 and 4, the enrichment function for the fiber is expressed as [41]:

$$\psi(\mathbf{x}) = \left[ \prod_{\alpha=1}^2 H(-\phi_\alpha) \right] \phi_c(\mathbf{x}) + \sum_{\alpha=1}^2 H(\phi_\alpha) d_\alpha(\mathbf{x}) \quad (6)$$

where,  $H$  denotes the Heaviside function; and  $d_\alpha(\mathbf{x}) = \|\mathbf{x} - \mathbf{x}_\alpha\|$  denotes the distance to the fiber tip.

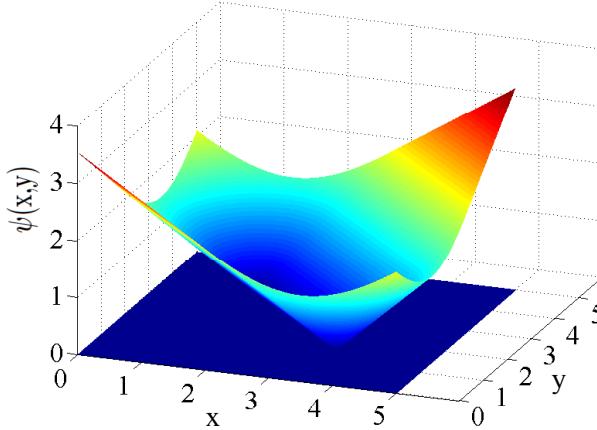


Figure 3: Short fiber inclusion enrichment function.

A three dimensional view of the enrichment function is shown in Fig. 3. Similar V-shaped enrichment functions have been employed in inclusion problems (e.g., [42]), with the exception of the treatment of the tip conditions. The inclusion of  $\psi(\mathbf{x})$  in the discretization of the displacement field incorporates a strain discontinuity mode along the fiber position. The displacements around the fiber can therefore be accurately captured without explicitly discretizing the fiber domain. The enrichment function defined in Eq. 6 ensures that the approximation basis captures the strain discontinuity but stays smooth otherwise around the sides and tips of the fiber. The enrichment function is nonzero everywhere in the composite domain except on the fiber.

The enrichment function leads to the enrichment of all nodes within the domain. This is clearly undesirable since away from the fiber, the enrichment does not enlarge the trial space spanned by the standard finite element shape functions but increases the size of the linear system and potentially lowers rank. We consider the enrichment only around a small domain around the fiber as is customary, and employ standard finite element shape functions in the remainder of the problem domain, as illustrated in Fig. 1c.

## 2.2 Debonding enrichment function

Similar to the fiber enrichment function, the debonding enrichment function  $\Upsilon$ , is defined using the fiber domain and tip level set functions. In contrast to the fiber enrichment, the debonding enrichment function introduces a discontinuity in the displacement field.

The shape of the debonding enrichment function is governed by the discontinuity function,  $\phi_p$ , which mimics the shape of the fiber-matrix debonding.  $\phi_p$  is taken to be a fourth order polynomial:

$$\phi_p(\mathbf{x}) = \sum_{k=0}^4 a_k s(\mathbf{x})^k \quad (7)$$

The following constraints are considered in the determination of the constants of the polynomial expression: (1) The ends of the fiber are taken to remain fully attached to the matrix (i.e.,  $\phi_p(s = \pm 1) = 0$ ); (2) Maximum debonding occurs at the center of the fiber (i.e.,  $d\phi_p/ds(s = 0) = 0$ ); and (3) The function is normalized such that the maximum value is unity at the center of the fiber (i.e.,  $\phi_p(s = 0) = 1$ ). Considering the constraints above, the discontinuity function is expressed as a function of a single shape parameter,  $\theta$  as:

$$\phi_p(\mathbf{x}) = 1 + \frac{\tan \theta}{2} s(\mathbf{x})^2 (1 - s(\mathbf{x})^2) - s(\mathbf{x})^2 (2 - s(\mathbf{x})^2) \quad (8)$$

where,  $\theta$  is the slope of the discontinuity at the tips of the fiber, controlling the shape of the discontinuity function:

$$\theta = \tan^{-1} \left( \frac{d\phi_p}{ds} \Big|_{s=-1} \right) \quad (9)$$

Figure 4a illustrates the effect of  $\theta$  on the shape of the discontinuity function  $\phi_p$ . When  $\theta$  is less than a threshold value (i.e.,  $\theta_{th}$ ) the discontinuity curve displays inflection points, which occur along the length of the fiber at positions that depend on the value of  $\theta$ . Above the threshold value, the discontinuity curve is convex. The threshold value for the chosen function form (Eq. 8) is  $\theta_{th} = 58^\circ$ . In the numerical verification studies provided in this manuscript, the shape parameter is set to  $\theta = 81^\circ$ . The shape parameter is chosen based on the shape of the debonding observed in direct finite element simulations of a short fiber inclusion subjected to remote tensile stress. In the presence of multiple nearby fibers, significant deviations from symmetry condition may occur. In case of a single fiber, the deviation from symmetry is typically slight. Furthermore, symmetry in the XFEM enrichment function does not necessarily imply that debonding must occur in a symmetric fashion and the proposed approach can capture asymmetric debonding as shown in examples below. This is because multiple enriched degrees of freedom are used in approximating the debonding of a single fiber (Eq. 1, third term on right hand side).

The debonding enrichment function for the fiber is then expressed in terms of the discontinuity function,  $\phi_\alpha(\mathbf{x})$  and  $\phi_c(\mathbf{x})$  as:

$$\Upsilon(\mathbf{x}) = \phi_p H(r(\phi_c)) \left( \prod_{\alpha=1}^2 H(-\phi_\alpha) \right) \quad (10)$$

where  $r = \pm \phi_c$  is the signed distance function as schematically illustrated in Fig. 2. A three dimensional visualization of the debonding enrichment function is shown in Fig. 4b.

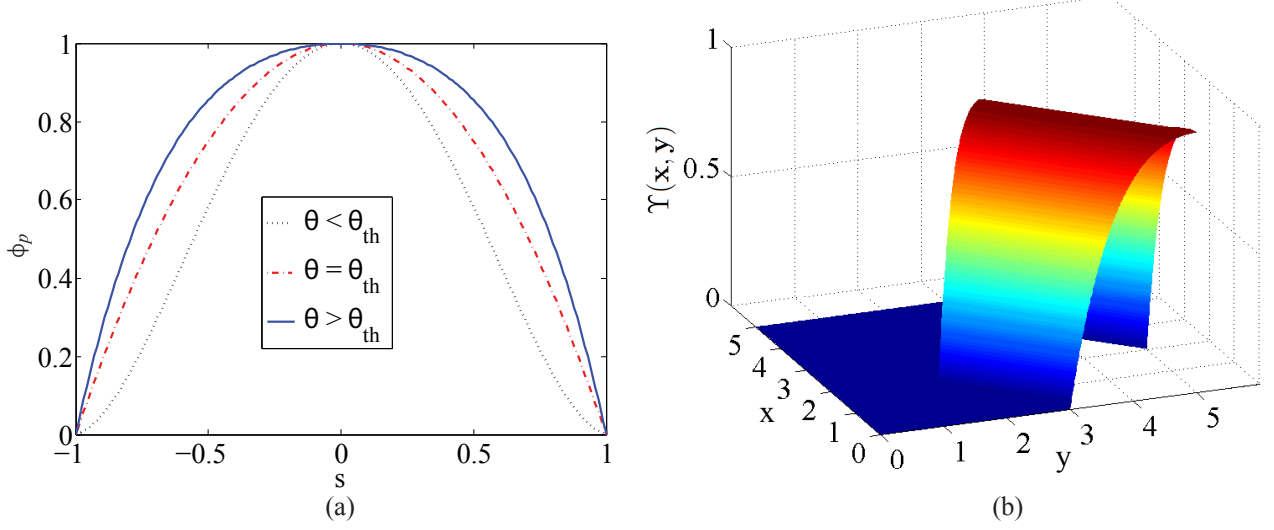


Figure 4: (a)  $\phi_p$  as a function of  $s$ , for  $\theta$  above, at and below the  $\theta_{th}$  value ; and (b) Short fiber inclusion debonding enrichment function.

### 3 Governing Equations and Model Formulation

Consider a matrix reinforced by  $n$  straight fibers. The length and the thickness of a fiber,  $\alpha$  is denoted as  $l_\alpha$  and  $t_\alpha$ , respectively ( $\alpha = 1, 2, \dots, n$ ). The mechanical equilibrium within the domain is expressed as:

$$\nabla \cdot \boldsymbol{\sigma}(\mathbf{x}, t) = 0; \quad \mathbf{x} \in \Omega \quad (11)$$

where,  $\boldsymbol{\sigma}$  is the stress tensor;  $\nabla(\cdot)$  the divergence operator; and  $\mathbf{x}$  and  $t$  are the space and time coordinates, respectively. Only quasi-static response is considered. The traction continuity across the fiber-matrix interface is given as:

$$[\![\mathbf{T}]\!] = [\![\boldsymbol{\sigma} \cdot \mathbf{n}]\!] = 0 \quad \mathbf{x} \in \Gamma_\alpha \equiv \partial\Omega_m \cap \partial\Omega_\alpha \quad \forall \alpha \quad (12)$$

in which,  $\mathbf{T}$  is the traction;  $\mathbf{n}$  the outward unit vector to a boundary; and  $[\![\cdot]\!]$  the jump operator. The domains of fiber  $\alpha$  and the matrix are denoted as  $\Omega_\alpha$  and  $\Omega_m$ , respectively. All fibers are taken to be fully embedded in the matrix with no intersection with exterior boundaries or with each other (i.e.,  $\Omega = \Omega_m \cup \bigcup_{\alpha=1}^n \Omega_\alpha$ ). The interface of the fiber  $\alpha$  with the matrix is denoted as  $\Gamma_\alpha$ . Tensor notation is employed in the formulation of the governing equations. The proposed formulation and implementation is limited to 2-D. While the general ideas remain relevant for the 3-D case, the 3-D implementation poses non-trivial challenges, and beyond the scope of this manuscript.

The exterior boundary conditions are expressed as:

$$\mathbf{u}(\mathbf{x}, t) = \tilde{\mathbf{u}}(\mathbf{x}, t); \quad \mathbf{x} \in \Gamma_u \quad (13)$$

$$\boldsymbol{\sigma} \cdot \mathbf{n} = \tilde{\mathbf{t}}(\mathbf{x}, t); \quad \mathbf{x} \in \partial\Gamma_t \quad (14)$$

in which,  $\tilde{\mathbf{u}}$  and  $\tilde{\mathbf{t}}$  are the prescribed boundary displacements and tractions defined on boundaries  $\Gamma_u$  and  $\Gamma_t$ , respectively, such that  $\Gamma_u \cap \Gamma_t = \emptyset$  and  $\partial\Omega = \Gamma_u \cup \Gamma_t$ . Since all fibers are embedded in the matrix, the displacement and traction boundaries of the problem domain,  $\Omega$ , coincide with those of  $\Omega_m$ .

The matrix is taken to progressively damage under applied mechanical loading, which is idealized using the continuum damage mechanics approach:

$$\boldsymbol{\sigma} = (1 - w(\mathbf{x}, t))\mathbf{L} : \boldsymbol{\epsilon}(\mathbf{x}, t) \quad (15)$$

in which,  $\boldsymbol{\epsilon}$  denotes the strain tensor; and  $w \in [0, 1]$  a scalar damage variable.  $w = 0$  and  $w = 1$  respectively denote the fully undamaged state and the complete loss of load carrying capacity at the material point. The focus is on the quasi-brittle behavior and therefore small strain theory is employed. The strain is taken to be the symmetric gradient of the displacement field ( $\boldsymbol{\epsilon} = \nabla^s \mathbf{u}$ ).  $\mathbf{L}$  denotes the tensor of elastic moduli of the matrix material, taken to be symmetric and positive definite. All fibers are assumed to remain elastic under the applied loading.

We develop the weak form equations for the governing equations at the limit, where the fiber aspect ratios are vanishingly small (i.e.,  $t_\alpha/l_\alpha \rightarrow 0$ ). Under this condition, the fiber domain is represented as sets of zero measure (i.e., line segments) and XFEM is employed to evaluate the governing equations. Using the standard procedure, the weak form of Eqs. 11-14 is expressed as follows:

$$\int_{\Omega_m} \boldsymbol{\sigma} : \delta\boldsymbol{\epsilon} d\Omega + \sum_{\alpha=1}^n \int_{\Omega_\alpha} \boldsymbol{\sigma} : \delta\boldsymbol{\epsilon} d\Omega + \sum_{\alpha=1}^n \int_{\Gamma_\alpha} \mathbf{T} \cdot \delta[\mathbf{u}] d\Gamma - \int_{\Gamma_t} \tilde{\mathbf{t}} \cdot \delta\mathbf{u} d\Gamma = 0 \quad (16)$$

where,  $\delta\mathbf{u}$  denotes the test function; and  $\delta\boldsymbol{\epsilon}$  the gradient of the test function. The traction continuity (i.e., Eq. 12) is weakly enforced, but the displacement field can develop discontinuity allowing the incorporation of progressive debonding between the fiber and the matrix.

Consider the local parameterization of the fiber domain,  $\Omega_\alpha$ , using the fiber normal and tangent vectors,  $\mathbf{n}_\alpha$  and  $\mathbf{t}_\alpha$ , respectively. Since fibers are straight, the normal and tangent vectors are constant for each fiber. Under the condition that aspect ratios of the fibers are very high, we assume that tractions along the two opposing faces in the thickness direction

are uniform:

$$\mathbf{T}^+(s) \cdot \mathbf{n}^+ \Big|_{\Gamma_\alpha^+} - \mathbf{T}^-(s) \cdot \mathbf{n}^- \Big|_{\Gamma_\alpha^-} = 0; \quad \mathbf{T}^+(s) \cdot \mathbf{t}^+ \Big|_{\Gamma_\alpha^+} - \mathbf{T}^-(s) \cdot \mathbf{t}^- \Big|_{\Gamma_\alpha^-} = 0 \quad (17)$$

Under these conditions, no shear stress or bending moment develops within the domain of the fiber. The stress that develops in the fiber is therefore only axial, and expressed as:

$$\boldsymbol{\sigma} = \sigma_f^\alpha(s) \mathbf{t}_\alpha \otimes \mathbf{t}_\alpha \quad (18)$$

The second term in Eq. 16 then becomes:

$$\int_{\Omega_\alpha} \boldsymbol{\sigma} : \delta \boldsymbol{\epsilon} d\Omega \simeq t_\alpha \int_{\Omega_\alpha} \sigma_f^\alpha \delta \epsilon_f^\alpha d\Omega \quad (19)$$

in which,  $\delta \epsilon_f^\alpha = \delta \boldsymbol{\epsilon} : \mathbf{t}_\alpha \otimes \mathbf{t}_\alpha$ . The axial stress in fiber  $\alpha$ , is taken to be proportional to the axial strain (i.e.,  $\sigma_f^\alpha = E_f \epsilon_f^\alpha$ ), where  $E_f$  is the elastic modulus of the fiber. Upon complete debonding between the fiber and the matrix, bending of the fiber may also develop. This deformation mode is not accounted for in the current manuscript.

The progressive debonding process between the fiber and the matrix is modeled through the third term in Eq. 16. We employ a simplification of the debonding process from the fiber to facilitate expression of progressive debonding using the enrichment function given in Eq. 10. For a short fiber embedded in a matrix under the traction conditions considered in Eq. 17, the debonding along the two faces of the fiber would occur simultaneously. In reality, the debonding is likely to initiate at a weak spot on one side of the fiber. Upon complete debonding at the weak side, the tractions along the opposing (unbonded) side relax. We further assume the tips of the fiber remain attached to the matrix. The internal boundary term then reduces to:

$$\int_{\Gamma_\alpha} \mathbf{T} \cdot \delta [\mathbf{u}] d\Gamma = \int_{\Gamma_\alpha^+} \mathbf{T} \cdot \delta [\mathbf{u}] d\Gamma \quad (20)$$

In the limit, where fiber aspect ratios tend to infinity, the weak form of the governing equations is expressed as:

$$\int_{\Omega} \boldsymbol{\sigma} : \delta \boldsymbol{\epsilon} d\Omega + \sum_{\alpha=1}^n t_\alpha E_f \int_{\Omega_\alpha} \epsilon_f^\alpha \delta \epsilon_f^\alpha d\Omega + \sum_{\alpha=1}^n \int_{\Gamma_\alpha} \mathbf{T} \cdot \delta [\mathbf{u}] d\Gamma - \int_{\Gamma_t} \tilde{\mathbf{t}} \cdot \delta \mathbf{u} d\Gamma = 0 \quad (21)$$

Since the domains of the fibers tend to a zero measure set, the domain of the matrix is taken to occupy the entire domain and the limits of the integral of the first term in Eq. 16 is set to  $\Omega$ .

### 3.1 Nonlocal damage model

The progressive damage and cracking within the matrix is modeled using continuum damage mechanics. It is also possible to model crack propagation using XFEM, particularly in the presence of pre-cracks. Other approaches that adaptively enrich the problem domain with cracks based on prescribed failure criteria have also been proposed (e.g. [20, 43, 44, 45]). One motivation in employing the continuum damage mechanics approach is that it can be extended to 3-D in a straightforward manner.

The basis of the continuum damage mechanics model is the idea of progressively degrading material until fracture, where the material no longer can carry load. The damage parameter  $w$ , characterizes the evolution of the secant moduli tensor of the material during the degradation process. The continuum damage mechanics model employed in this manuscript is regularized to eliminate the well known issues of spurious strain localization and mesh dependency. A number of approaches exist to eliminate the mesh dependency problem including nonlocal modeling of gradient and integral type, viscous regularization, crack band method, variational multiscale method and others (e.g. [46, 47, 48, 49, 50, 51, 52]). In this study, the nonlocal regularization of integral type is employed.

At an arbitrary material point  $\hat{\mathbf{x}}$ , the state of damage follows a smooth function,  $g$ :

$$w(\hat{\mathbf{x}}, t) = g(k(\hat{\mathbf{x}}, t)) \quad (22)$$

in which,  $g(k)$  is taken to follow an arctangent law as a function of a history dependent parameter,  $k$  as:

$$g(k) = \frac{\arctan(a k(\hat{\mathbf{x}}, t) - b) + \arctan(b)}{\frac{\pi}{2} + \arctan(b)} \quad (23)$$

where,  $a$  and  $b$  are parameters that characterize the evolution of damage and control ductility and strength.  $k$  indicates the maximum past value of the nonlocal damage equivalent strain,  $\hat{v}$ :

$$k(\hat{\mathbf{x}}, t) = \max_{\tau \in [0, t]} (\langle \hat{v}(\hat{\mathbf{x}}, \tau) - v_{\text{ini}} \rangle) \quad (24)$$

in which,  $v_{\text{ini}}$  is the threshold value of  $\hat{v}$ , below which damage does not progress; and  $\langle \cdot \rangle = ((\cdot) + |\cdot|)/2$  the Macaulay brackets. The nonlocal damage equivalent strain is expressed as a function of the local damage equivalent strain,  $v$ , using the following equation:

$$\hat{v}(\hat{\mathbf{x}}) = \frac{\int_{\Omega} \lambda(\mathbf{x}, \hat{\mathbf{x}}) v(\mathbf{x}, t) d\mathbf{x}}{\int_{\Omega} \lambda(\mathbf{x}, \hat{\mathbf{x}}) d\mathbf{x}} \quad (25)$$

The local equivalent strain is taken as a function of the principle strains as proposed by Prisco

and Mazars [53]:

$$v(\hat{\mathbf{x}}, t) = \sqrt{\sum_{I=1}^2 \langle \epsilon_I(\hat{\mathbf{x}}, t) \rangle^2} \quad (26)$$

where  $\epsilon_I$  are the principle strains. The Macaulay brackets incorporate the tension-compression anisotropy. Under compressive strain, the damage is not allowed to grow. In this manuscript, the verification studies focus only on the tension failure. The nonlocal weighting of the damage equivalent strain,  $\lambda$  is expressed using the Wendland Radial Basis Function [54]:

$$\lambda(\mathbf{x}, \hat{\mathbf{x}}) = \begin{cases} \left(1 - \frac{\|\mathbf{x} - \hat{\mathbf{x}}\|}{l_c}\right)^4 \left(4 \frac{\|\mathbf{x} - \hat{\mathbf{x}}\|}{l_c} + 1\right) & \|\mathbf{x} - \hat{\mathbf{x}}\| \leq l_c \\ 0 & \|\mathbf{x} - \hat{\mathbf{x}}\| > l_c \end{cases} \quad (27)$$

in which,  $l_c$  denotes the characteristic length defining the span of the radial basis.

In the context of fibrous composites, the domains of the fiber, whether modeled as zero measure or not, potentially constitute a boundary in the application of the nonlocal weighting. In the present study, the nonlocal averaging is applied without considering the fiber domains as boundaries. In all verification studies considered below, similar strategy is employed in the reference simulations as well.

### 3.2 Cohesive law

The progressive debonding between the fiber and the matrix is modeled by prescribing cohesive zone laws. In the numerical verification and studies included in this manuscript an exponential and a bilinear cohesive law are considered. The cohesive law at the interface describes the relationship between the surface traction and material separation between the surfaces, representing the physical deterioration occurring at the interface. The proposed computational approach differs considerably from traditional cohesive zone modeling, which entails incorporation of cohesive elements between standard finite elements. Since the positions of the fibers do not necessarily comply with the underlying domain discretization, the proposed approach does not include cohesive elements.

The debonding enrichment function is taken to have a parabolic shape along the fiber as described in Eq. 8. The actual debonding may deviate from the parabolic shape since multiple degrees of freedom are employed to discretize the fiber-matrix debonding (i.e., Eq. 1).

The exponential cohesive law employed in this manuscript is derived from an interface potential as proposed by Xu and Needleman [55]. The interface tractions are expressed as:

$$\mathbf{T} = \frac{\partial \Phi([\mathbf{u}])}{\partial [\mathbf{u}]} \quad (28)$$

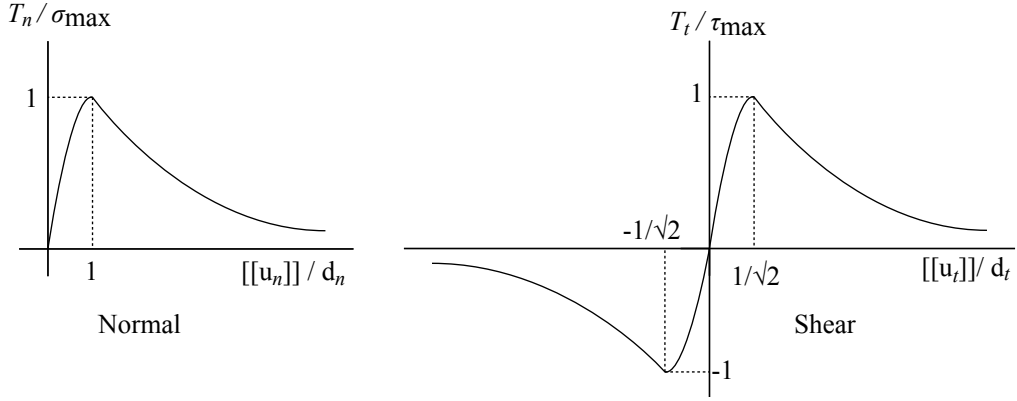


Figure 5: The exponential traction-separation laws by Xu and Needleman [56].

in which, the interface potential,  $\Phi$  is a function of displacement jumps normal and tangential to the fiber directions [56]:

$$\Phi(\|u\|) = \Phi_n + \Phi_n \exp(-\frac{\|u_n\|}{d_n}) \left\{ \left[ 1 - y + \frac{\|u_n\|}{d_n} \right] \frac{1-q}{y-1} - \left[ q + \frac{y-q}{y-1} \frac{\|u_n\|}{d_n} \right] \exp\left(-\frac{\|u_t\|^2}{d_t^2}\right) \right\} \quad (29)$$

in which,  $\|u_n\|$  and  $\|u_t\|$  are the components of the displacement jump vector along the normal and tangential directions, respectively;  $d_n$  and  $d_t$  the normal and tangential cohesive characteristic separation lengths, respectively;  $y = \|u_n\|'/d_n$ ;  $\|u_n\|'$  the magnitude of normal displacement jump when complete shear failure has taken place;  $q = \Phi_t/\Phi_n$ ;  $\Phi_n$  the normal surface potential energy; and  $\Phi_t$  is the tangential surface potential energy.  $\Phi_n$  and  $\Phi_t$  represent the areas under the normal and tangential traction-separation curves, respectively. The normalized exponential normal and tangential traction-separation behavior is illustrated in Fig. 5.

Differentiating Eq. 29 with respect to the components of the displacement jump normal and tangential to the fiber direction, the components of the traction vector are obtained:

$$T_n = \frac{\Phi_n}{d_n} \exp\left(-\frac{\|u_n\|}{d_n}\right) \left\{ \frac{\|u_n\|}{d_n} \exp\left(-\frac{\|u_t\|^2}{d_t^2}\right) + \frac{1-q}{y-1} \left[ 1 - \exp\left(-\frac{\|u_t\|^2}{d_t^2}\right) \right] \left[ y - \frac{\|u_n\|}{d_n} \right] \right\} \quad (30)$$

$$T_t = 2 \left( \frac{\Phi_n \|u_t\|}{d_t^2} \right) \left\{ q + \frac{1-q}{y-1} \frac{\|u_n\|}{d_n} \right\} \exp\left(-\frac{\|u_n\|}{d_n}\right) \exp\left(-\frac{\|u_t\|^2}{d_t^2}\right) \quad (31)$$

In some of the numerical verification studies below, we also consider a simpler bilinear

cohesive law. In this model, the uncoupled tangential and normal tractions are expressed as:

$$T_n(\llbracket u_n \rrbracket) = \begin{cases} \frac{\llbracket u_n \rrbracket}{d_n} \sigma_{\max} & d_n \geq \llbracket u_n \rrbracket \geq 0 \\ \frac{\sigma_{\max}}{d_n^{\text{crit}} - d_n} (d_n^{\text{crit}} - \llbracket u_n \rrbracket) & d_n^{\text{crit}} \geq \llbracket u_n \rrbracket \geq d_n \\ 0 & \llbracket u_n \rrbracket \geq d_n^{\text{crit}} \end{cases} \quad (32)$$

$$T_t(\llbracket u_t \rrbracket) = \begin{cases} \frac{\llbracket u_t \rrbracket}{d_t} \tau_{\max} & d_t \geq \llbracket u_t \rrbracket \geq 0 \\ \frac{\tau_{\max}}{d_t^{\text{crit}} - d_t} (d_t^{\text{crit}} - \llbracket u_t \rrbracket) & d_t^{\text{crit}} \geq \llbracket u_t \rrbracket \geq d_t \\ 0 & \llbracket u_t \rrbracket \geq d_t^{\text{crit}} \end{cases} \quad (33)$$

where;  $d_n$  and  $d_t$  are described identical to the exponential law;  $\sigma_{\max}$  and  $\tau_{\max}$  denote the ultimate normal and tangential tractions, respectively;  $d_n^{\text{crit}}$  and  $d_t^{\text{crit}}$  are the maximum normal and tangential displacement jumps, respectively.

The two cohesive zone laws considered above are intrinsic, i.e., contains a linear "hardening" portion. For certain problems, the intrinsic laws were found to lead to spurious softening [57] and numerical instability [58], compared to the extrinsic cohesive laws. Despite numerical difficulties, the intrinsic laws have been much more popular due to the simplicity of their implementation into standard finite element codes using cohesive zone elements. In the current approach, since the cohesive behavior is introduced through enrichment functions, the implementation of extrinsic laws do not significantly differ from intrinsic laws. The intrinsic laws are considered here, due to the availability of commercial software that serves as reference models in numerical verifications discussed below.

## 4 Computational Formulation and Implementation

The governing equations (Eqs. 11-21) are discretized and evaluated based on the extended finite element method following the standard Ritz-Galerkin procedure. In what follows, the matrix notation is employed in the formulations for convenience. The weak form of the governing equation (Eq. 21) is re-written in the matrix form as:

$$\int_{\Omega} \delta \boldsymbol{\epsilon}^T \boldsymbol{\sigma} d\Omega - \int_{\Gamma_t} \delta \mathbf{u}^T \tilde{\mathbf{t}} d\Gamma + \sum_{\alpha=1}^n t_{\alpha} E_f \int_{\Omega_{\alpha}} \epsilon_f^{\alpha} \delta \epsilon_f^{\alpha} d\Omega + \sum_{\alpha=1}^n \int_{\Gamma_{\alpha}} \delta \llbracket \mathbf{u} \rrbracket^T \mathbf{T} d\Gamma = 0 \quad (34)$$

where, the superscript  $T$  indicates transpose.

The discretization of the displacement field follows Eq. 1, and using the Bubnov-Galerkin approach, the discretization of the test function is similar to that of the trial function. In

contrast to the standard finite element approach, the mesh does not necessarily conform to the fiber domains, i.e., the position of the fibers are independent of the mesh. The first term in Eq. 34 becomes:

$$\int_{\Omega} \delta \epsilon^T \boldsymbol{\sigma} d\Omega = \sum_{e=1}^{n_e} \int_{\Omega_e} \delta \epsilon^T \boldsymbol{\sigma} d\Omega \quad (35)$$

in which,  $n_e$  is the total number of elements discretizing the domain; and  $\Omega_e$  the domain of the element,  $e$ . Substituting the test and trial function discretizations into Eq. 35, the element level integral is expressed as:

$$\int_{\Omega_e} \delta \epsilon^T \boldsymbol{\sigma} d\Omega = (\mathbf{V}^e)^T \int_{\Omega_e} (\mathbf{B}^e)^T \boldsymbol{\sigma} (\mathbf{U}^e) d\Omega \quad (36)$$

where,  $\mathbf{U}^e$  and  $\mathbf{V}^e$  are the nodal coefficient vectors of the trial and test functions in element,  $e$ , respectively:

$$\mathbf{U}^e = \left\{ \hat{\mathbf{u}}^e; \hat{\mathbf{c}}^e; \hat{\mathbf{d}}^e \right\}; \quad \mathbf{V}^e = \left\{ \delta \hat{\mathbf{u}}^e; \delta \hat{\mathbf{c}}^e; \delta \hat{\mathbf{d}}^e \right\} \quad (37)$$

in which, a semicolon implies that the construction forms a column vector. The three components in the nodal coefficient vectors correspond to the standard, fiber enrichment and the jump enrichment degrees of freedom respectively:

$$\hat{\mathbf{u}}^e = \left\{ \hat{\mathbf{u}}_1^e; \hat{\mathbf{u}}_2^e; \dots; \hat{\mathbf{u}}_{n_n^e}^e \right\} \quad \hat{\mathbf{c}}^e = \left\{ \hat{\mathbf{c}}_1^e; \hat{\mathbf{c}}_2^e; \dots; \hat{\mathbf{c}}_{n_{\text{en}}^e}^e \right\} \quad \hat{\mathbf{d}}^e = \left\{ \hat{\mathbf{d}}_1^e; \hat{\mathbf{d}}_2^e; \dots; \hat{\mathbf{d}}_{n_{\text{en}}^e}^e \right\} \quad (38)$$

where,  $\hat{\mathbf{u}}_a^e$ ,  $\hat{\mathbf{c}}_a^e$  and  $\hat{\mathbf{d}}_a^e$  are the vectors of unknown coefficients for standard and extended degrees of freedom at element,  $e$  and node  $a$ ; and  $n_n^e$  and  $n_{\text{en}}^e$  the number of standard and enriched nodes within element,  $e$ , respectively. The components of  $\mathbf{V}^e$  are similarly defined.

$$\mathbf{B}^e = \left\{ \hat{\mathbf{B}}_1^e, \hat{\mathbf{B}}_2^e, \dots, \hat{\mathbf{B}}_{n_n^e}^e, \bar{\mathbf{B}}_1^e, \bar{\mathbf{B}}_2^e, \dots, \bar{\mathbf{B}}_{n_{\text{en}}^e}^e, \tilde{\mathbf{B}}_1^e, \tilde{\mathbf{B}}_2^e, \dots, \tilde{\mathbf{B}}_{n_{\text{en}}^e}^e \right\} \quad (39)$$

in which, the gradient terms are expressed as:

$$\hat{\mathbf{B}}_a^e = \begin{bmatrix} N_{a,x}^e & 0 \\ 0 & N_{a,y}^e \\ N_{a,y}^e & N_{a,x}^e \end{bmatrix}; \quad \bar{\mathbf{B}}_a^e = \begin{bmatrix} (N_a^e \psi),_x & 0 \\ 0 & (N_a^e \psi),_y \\ (N_a^e \psi),_y & (N_a^e \psi),_x \end{bmatrix}; \quad \tilde{\mathbf{B}}_a^e = \begin{bmatrix} (N_a^e \Upsilon),_x & 0 \\ 0 & (N_a^e \Upsilon),_y \\ (N_a^e \Upsilon),_y & (N_a^e \Upsilon),_x \end{bmatrix} \quad (40)$$

where, a subscript followed by a comma indicates differentiation. The first term in Eq. 34 is then written in the matrix form as:

$$\mathbf{V}^T \mathbf{f}_{\text{int},1}(\mathbf{U}) \quad (41)$$

in which, the internal force component is obtained by assembling the corresponding element

matrices:

$$\mathbf{f}_{\text{int},1}(\mathbf{U}) = \sum_{e=1}^{n_e} \int_{\Omega_e} (\mathbf{B}^e)^T \boldsymbol{\sigma}(\mathbf{U}^e) d\Omega \quad (42)$$

$\mathbf{U}$  and  $\mathbf{V}$  are obtained by assembling the corresponding element vectors. Where  $\boldsymbol{\sigma}$  at an arbitrary position  $\hat{\mathbf{x}}$  is defined in the discretized form as:

$$\boldsymbol{\sigma} = (1 - w) \mathbf{L} \mathbf{B}^e \mathbf{U}^e \quad (43)$$

Decomposing the boundary integral into its elemental components, the external force contribution in Eq. 34 is expressed as:

$$\int_{\Gamma_t} \delta \mathbf{u}^T \tilde{\mathbf{t}} d\Gamma = \mathbf{V}^T \mathbf{f}_{\text{ext}} \quad (44)$$

in which, the external force vector is obtained through the assembly of the elemental contributions:

$$\mathbf{f}_{\text{ext}}^e = \int_{\Gamma_t^e} \mathbf{f}^e(\mathbf{x}) d\Gamma; \quad e \in \mathcal{I}^t \quad (45)$$

where,  $\mathcal{I}^t$  denotes the index set of elements along the traction boundary,  $\Gamma_t$ ;  $\Gamma_t^e$  the part of the traction boundary approximated by element  $e$ ; and:

$$\mathbf{f}^e = \left\{ \hat{\mathbf{f}}_1^e; \hat{\mathbf{f}}_2^e; \dots; \hat{\mathbf{f}}_{n_n^e}^e; \bar{\mathbf{f}}_1^e; \bar{\mathbf{f}}_2^e; \dots; \bar{\mathbf{f}}_{n_{\text{en}}^e}^e; \tilde{\mathbf{f}}_1^e; \tilde{\mathbf{f}}_2^e; \dots; \tilde{\mathbf{f}}_{n_{\text{en}}^e}^e \right\} \quad (46)$$

$$\hat{\mathbf{f}}_a^e(\mathbf{x}) = N_a^e(\mathbf{x}) \tilde{\mathbf{t}}(\mathbf{x}); \quad \tilde{\mathbf{f}}_a^e(\mathbf{x}) = \hat{\mathbf{f}}_a^e(\mathbf{x}) \psi(\mathbf{x}); \quad \tilde{\mathbf{f}}_a^e(\mathbf{x}) = \hat{\mathbf{f}}_a^e(\mathbf{x}) \Upsilon(\mathbf{x}) \quad (47)$$

## 4.1 Fiber deformation

The third term in Eq. 34 accounts for the deformation of the fibers. The integral term is expressed in terms of its components that lie in each enriched element as:

$$\int_{\Omega_\alpha} \epsilon_f^\alpha \delta \epsilon_f^\alpha d\Omega = \sum_{e=1}^{n_e^\alpha} \int_{\Omega_\alpha^e} \epsilon_f^\alpha \delta \epsilon_f^\alpha d\Omega \quad (48)$$

in which,  $n_e^\alpha$  denotes the number of fully enriched elements that contains a part of the fiber,  $\alpha$ . We assume that the fiber will deform uniformly within each element. Therefore, the axial strain of fiber,  $\alpha$ , can be defined as:

$$\epsilon_f^\alpha = \frac{[\mathbf{u}(\mathbf{x}_2^{\alpha e}) - \mathbf{u}(\mathbf{x}_1^{\alpha e})] \cdot \mathbf{t}_\alpha}{l_{\alpha e}}; \quad \mathbf{x} \in \Omega_\alpha^e \quad (49)$$

where  $\mathbf{x}_1^{\alpha e}$  and  $\mathbf{x}_2^{\alpha e}$  are the entry and exit positions of the fiber on the enriched element; the length of the fiber segment that lies within the element is denoted as  $l_{\alpha e} = \|\mathbf{x}_2^{\alpha e} - \mathbf{x}_1^{\alpha e}\|$ ; and  $\mathbf{t}_\alpha$

is the tangent vector on the fiber domain. When the fiber crosses the domain of the element, the fiber entry and exit positions are on the element edges. If the domain of the fiber ends within the element, the end position of the fiber segment coincides with the fiber tip.

Substituting Eq. 49 to the third term in Eq. 34 leads to:

$$\begin{aligned} t_\alpha E_f \int_{\Omega_e^\alpha} \epsilon_f^\alpha \delta \epsilon_f^\alpha d\Omega &= \frac{t_\alpha E_f}{l_{\alpha e}} [(\mathbf{u}(\mathbf{x}_2^{\alpha e}) - \mathbf{u}(\mathbf{x}_1^{\alpha e})) \cdot \mathbf{t}_\alpha] [(\delta \mathbf{u}(\mathbf{x}_2^{\alpha e}) - \delta \mathbf{u}(\mathbf{x}_1^{\alpha e})) \cdot \mathbf{t}_\alpha] \\ &= (\delta \hat{\mathbf{u}}^e)^T \check{\mathbf{K}}_e^{\alpha s} \hat{\mathbf{u}}^e \quad (50) \end{aligned}$$

where,

$$\check{\mathbf{K}}_e^{\alpha s} = \frac{t_\alpha E_f}{l_{\alpha e}} \begin{bmatrix} \check{\mathbf{K}}_{e,11}^{\alpha s} & \check{\mathbf{K}}_{e,12}^{\alpha s} & \dots & \check{\mathbf{K}}_{e,1n_n^e}^{\alpha s} \\ \check{\mathbf{K}}_{e,21}^{\alpha s} & \check{\mathbf{K}}_{e,22}^{\alpha s} & & \vdots \\ \vdots & & \ddots & \vdots \\ \check{\mathbf{K}}_{e,n_n^e 1}^{\alpha s} & \dots & \dots & \check{\mathbf{K}}_{e,n_n^e n_n^e}^{\alpha s} \end{bmatrix} \quad (51)$$

An individual component of the stiffness matrix is written as:

$$\check{\mathbf{K}}_{e,ab}^{\alpha s} = [N_b^e(\mathbf{x}_2^{\alpha e}) - N_b^e(\mathbf{x}_1^{\alpha e})] [N_a^e(\mathbf{x}_2^{\alpha e}) - N_a^e(\mathbf{x}_1^{\alpha e})] (\mathbf{t}_\alpha \otimes \mathbf{t}_\alpha) \quad (52)$$

The internal contribution from the second term in Eq. 34 then becomes:

$$\mathbf{f}_{\text{int},2}^\alpha(\mathbf{U}) = \check{\mathbf{K}}^\alpha \mathbf{U} \quad (53)$$

where, the contribution can be computed using the standard assembly operation:

$$\check{\mathbf{K}}^\alpha = \sum_{e=1}^{n_e^\alpha} \check{\mathbf{A}}_e \check{\mathbf{K}}_e^\alpha \quad (54)$$

The stiffness matrix is nonzero only for the standard degrees of freedom, since the enrichment functions vanish on the domain of the fiber:

$$\check{\mathbf{K}}_e^\alpha = \begin{bmatrix} \check{\mathbf{K}}_e^{\alpha s} & \mathbf{0} \\ \mathbf{0} & \mathbf{0} \end{bmatrix} \quad (55)$$

## 4.2 Cohesive interfaces

The fourth component of Eq. 34 that accounts for the progressive debonding between the fibers and the matrix is expressed in terms of the jump enrichment degrees of freedom. For an

arbitrary fiber,  $\alpha$ :

$$\int_{\Gamma_\alpha} (\delta[\![\mathbf{u}]\!])^T \mathbf{T}([\![\mathbf{u}]\!]) d\Gamma = (\delta\hat{\mathbf{d}})^T \int_{\Gamma_\alpha} (\mathbf{P}^\alpha)^T \mathbf{T}(\hat{\mathbf{d}}) d\Gamma = (\delta\hat{\mathbf{d}})^T \mathbf{f}_{\text{int},3}^{d\alpha}(\hat{\mathbf{d}}) \quad (56)$$

in which,  $\mathbf{P}^\alpha$  includes the shape functions for the jump enrichments:

$$\mathbf{P}^\alpha = \left\{ \mathbf{P}_1^\alpha, \mathbf{P}_2^\alpha, \dots, \mathbf{P}_{n_{\text{en}}^\alpha}^\alpha \right\}; \quad \mathbf{P}_a^\alpha = N_{\mathcal{I}_a^\alpha}(\mathbf{x}) \Upsilon(\mathbf{x}) \begin{bmatrix} 1 & 0 \\ 0 & 1 \end{bmatrix} \quad (57)$$

where,  $n_{\text{en}}^\alpha$  denotes the number of nodes enriched for fiber,  $\alpha$  and  $\mathcal{I}^\alpha$  the corresponding nodal index set. The debonding enrichment term is then assembled into a force vector contribution (i.e.,  $\mathbf{V}^T \mathbf{f}_{\text{int},3}^\alpha(\mathbf{U})$ ):

$$\mathbf{f}_{\text{int},3}^\alpha = \left\{ \mathbf{0}; \mathbf{0}; \mathbf{f}_{\text{int},3}^{d\alpha} \right\} \quad (58)$$

The null vectors indicate that the internal force contribution is only due to the jump degrees of freedom. Including the three internal force contributions as well as the external force, the resulting equilibrium is expressed in terms of a system of nonlinear equations of the form:

$$\phi(\mathbf{U}) = \mathbf{f}_{\text{int}}(\mathbf{U}) - \mathbf{f}_{\text{ext}} = 0 \quad (59)$$

where,

$$\mathbf{f}_{\text{int}}(\mathbf{U}) = \mathbf{f}_{\text{int},1} + \sum_{\alpha=1}^n (\mathbf{f}_{\text{int},2}^\alpha + \mathbf{f}_{\text{int},3}^\alpha) \quad (60)$$

Equation 60 is evaluated incrementally using the Newton-Raphson method.

### 4.3 Numerical integration

The domain is discretized using four different element types as illustrated in Fig. 1c: (1) Far field elements with no enrichment; (2) elements with partial enrichment; (3) fully enriched elements crossed by the fiber; and (4) fully enriched elements partially crossed by the fiber that contain the fiber tip. The treatment of the enrichment and the numerical integration differ for different element types. The enrichment domain in XFEM is typically chosen either based on the geometry or the discretization. The geometry-based approach considers full enrichment in all elements within a specified radius of the interface. The geometry based approach is particularly suitable for modeling of cracks, in which the stress fields around the crack tip, varies as a function of the distance from the tip. In this study, the enrichment domain is chosen based on the discretization since the enrichments functions remain local.

The integration rules for all cases of enrichment are as follows:

1. Far field elements: No enrichment, standard integration orders apply since no additional

functions employed in these elements.

2. Partially enriched elements: Some nodes include enrichment functions but no intra-element strain discontinuity exists. While high order integration rule could increase the accuracy, standard integration is employed for efficiency.
3. Fully enriched elements entirely crossed by the fiber: The elements are split by the fiber. Using Delaunay triangulation, each split part is decomposed into triangular sub-elements. Higher order integration rules are used to capture high order enrichment fields within each sub-element.
4. Fully enriched elements that contain fiber tips: The elements are split along the normal direction at the fiber tip and along the fiber direction. Using Delaunay triangulation, each split part is decomposed into triangular sub-elements. High order integration rules are used in each sub-element. The element splitting at the fiber normal ensures that the components of the enrichment function that pertain to the fiber tip and fiber level sets are integrated separately.

In full enrichment cases, triangular sub-elements aligned with the fiber faces are used in the integration of a 2-D quadrilateral. The triangular sub-elements contain three integration points and use the standard Gauss quadrature rules. Gauss quadrature rule with 4 integration points is performed in the partially enriched elements and the far-field elements [59]. The partially enriched elements do not have sub elements since the fiber does not cross through the element.

The integration of the cohesive interface (Eq. 56) is performed using Gauss quadrature, but independent of the domain discretization. The fiber-matrix interface  $\Gamma_\alpha$  is decomposed into a small number of segments depending on the length of the fiber,  $l_\alpha$ . Within each fiber segment, a 12-point quadrature rule is employed.

#### 4.4 Treatment of partially enriched elements

The treatment of the partially enriched elements has an effect on the accuracy and convergence of XFEM models [60], because within partially enriched elements the partition of unity property no longer holds and the affine transformations (e.g. constant strain modes) cannot be represented exactly. Various solution strategies exist to alleviate these problems (e.g. [61, 62]). Fries [60] modified the enrichment functions with a ramp function that has a local support within the partially enriched element, and applied the enrichment to all nodes of the partially enriched element using the modified enrichment function. In the current study, a similar modification of the enrichment function is considered. Let  $\hat{\psi}(\mathbf{x})$  and  $\hat{\Gamma}(\mathbf{x})$  denote the modified enrichment functions within a partially enriched finite element:

$$\hat{\psi}(\mathbf{x}) = \sum_{b \in \mathcal{I}_e} N_b(\mathbf{x}) \psi(\mathbf{x}); \quad \mathbf{x} \in \Omega_e \quad (61)$$

$$\hat{\Upsilon}(\mathbf{x}) = \sum_{c \in \mathcal{I}_e} N_c(\mathbf{x}) \Upsilon(\mathbf{x}); \quad \mathbf{x} \in \Omega_e \quad (62)$$

where,  $\mathcal{I}_e$  are the nodes in the partially enriched element,  $\Omega_e$ , that are connected to fully enriched elements. The modified enrichment function is active at all nodes of the partially enriched element:

$$\mathbf{u}^e(\mathbf{x}) = \sum_{a=1}^{n_n^e} N_a^e(\mathbf{x}) \hat{\mathbf{u}}_a^e + \sum_{b=1}^{n_n^e} N_b^e(\mathbf{x}) \hat{\psi}(\mathbf{x}) \hat{\mathbf{c}}_b^e + \sum_{c=1}^{n_n^e} N_c^e(\mathbf{x}) \hat{\Upsilon}(\mathbf{x}) \hat{\mathbf{d}}_c^e \quad (63)$$

in which, all pertinent variables are defined in the partially enriched element are indicated by the superscript,  $e$ .

## 5 Numerical Examples

In this section, we present numerical examples to demonstrate the performance of the proposed XFEM model in evaluating the response of short fiber reinforced composites in a two-dimensional setting. The first example assesses the behavior of multiple random short deformable fibers embedded in an elastic matrix with perfect interfacial cohesion. The second example illustrates the accuracy characteristics of the method using a single fiber inclusion embedded in a matrix with progressive fiber-matrix debonding. The third example reviews a domain with two fiber inclusions to demonstrate its capabilities in the presence of matrix cracking modeled using nonlocal continuum damage mechanics. The fourth example evaluates the performance of random short fiber composites with varying interface properties.

### 5.1 Elastic response of fibrous composite

This section investigates the response of two-dimensional random short fiber composites in which the fibers are fully bonded to the matrix. No fiber-matrix debonding occurs and the constituents are taken to deform elastically. The problem domain is taken to be 100 mm by 100 mm. The Young's modulus and Poisson's ratio of the matrix material are 14 GPa and 0.3, respectively. The Young's modulus, Poisson's ratio and the thickness of the fibers are 207 GPa, 0.3 and 7  $\mu\text{m}$ , respectively. Fibers are assigned lengths randomly with a mean of 5 mm ( $\pm 1$  mm). The domain was subjected to displacement controlled tensile loading at the right edge. Symmetry boundary conditions are imposed on the left and bottom edges.

Volume element sets with specified weight fractions of between 0.025% and 0.15% were generated and subjected to uniform uniaxial displacement. The overall composite stiffness

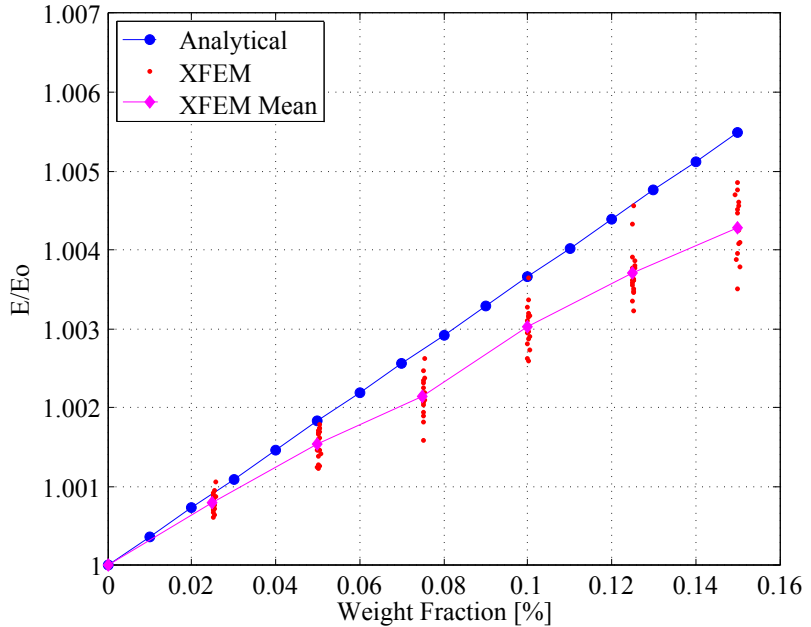


Figure 6: Elastic modulus ratio of fibrous composite.

was computed as a function of fiber weight fraction. The fibers were positioned such that no element within the domain is enriched by more than a single fiber. 6 different weight fractions were considered. Composite behavior variability is due to two distinct factors: (a) the natural variability due to the random positioning of the fibers within the matrix in each realization; and (b) the effect of overall volume element size (i.e., statistical representativeness of the volume element). The effect of the second factor is minimized by choosing large enough representative volumes. This size of the volumes are determined as the smallest matrix volume beyond which the modulus variability does not significantly change.

Figure 6 illustrates the normalized composite modulus as a function of weight fraction computed by the proposed approach and with the analytical model for a two dimensional randomly oriented fiber composite provided by Pan [63]. At each weight fraction, 20 randomly generated microstructures are simulated with the proposed model on a uniform grid of 10,000 elements. The results of the proposed XFEM formulation are plotted along with the mean value at each weight fraction. The results of the proposed model display a variation from configuration to configuration at a fixed weight fraction but the discrepancy between the mean and the analytical model is within 0.1% (computed as the error of absolute moduli rather than the normalized moduli).

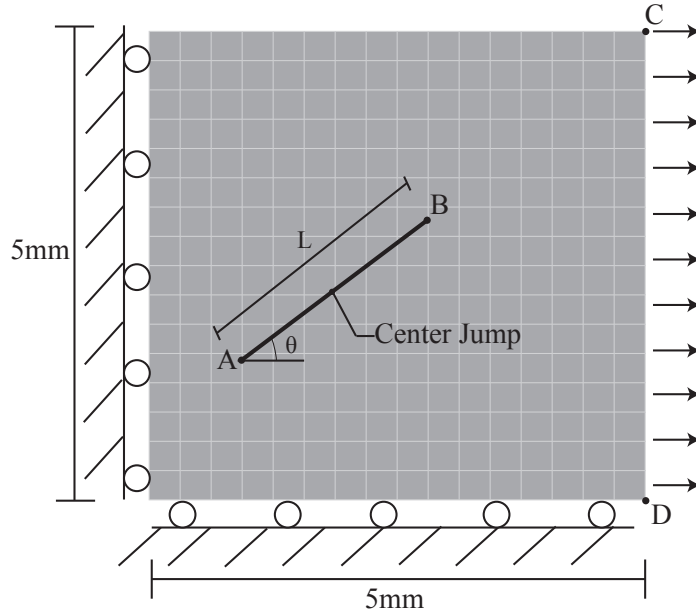


Figure 7: Geometry and boundary conditions of the single fiber inclusion example.

## 5.2 Single fiber inclusion example

The proposed formulation is verified against the finite element method using a series of simulations of a matrix enriched with a single fiber. The schematic representation of the model problem is shown in Fig. 7. The size of the domain is 5 mm by 5 mm and the fiber length, varies between 1-2.5 mm. The domain is subjected to uniform uniaxial tensile loading applied at the right edge. The fiber is placed such that it results in a non-uniform deformation and stress distribution within the matrix. The Young's modulus and Poisson's ratio of the matrix material are 14 GPa and 0.3, respectively. The Young's modulus, Poisson's ratio and thickness of the fiber material are 207 GPa, 0.3 and 7  $\mu\text{m}$ , respectively.

A bi-linear cohesive zone law (defined in Eq. 32 and Eq. 33) is employed for both the XFEM and the reference simulations. The peak normal traction and normal cohesive characteristic separation length are set to 8 MPa and 0.01591 mm, respectively. The peak shear traction and shear cohesive characteristic separation length are 1.8 MPa and 0.01141 mm, respectively. The maximum cohesive separation length is taken as 0.08 mm under pure normal and pure shear loading [55, 64].

In the proposed approach, the fiber is idealized as a 1-D line segment with cross sectional area and length properties. The discretization of the domain uses uniform grids ranging from 1,600 elements up to approximately 62,500 elements with corresponding element sizes of  $h=0.0625$  mm and 0.02 mm, respectively. The reference model consists of a very fine and nonuniform (to conform to the fiber domain) discretization, in which the fiber is explicitly

modeled as a two dimensional solid. The fiber domain is modeled using a very fine grid with approximately element size of  $1 \mu\text{m}$ . The reference model utilizes  $1 \mu\text{m}$  wide cohesive zone elements that lay along the interface between the fiber and the matrix. The reference model discretization results in approximately 200,000 - 630,000 elements. The simulations confirmed that the response is very accurately captured at such high levels of discretization.

Figure 8 shows the point-wise displacement errors of the proposed model with respect to the reference simulations at peak cohesive tractions (Figs. 8a, 8c, 8e) and at the point of full separation (Figs. 8b, 8d, 8f), respectively. At the point of full separation, the fiber and the matrix are completely debonded from each other at one side of the fiber and the interfacial tractions vanish. The accuracy is assessed at five different locations as illustrated in Fig. 7. Points A, B, C, D refer to the left fiber tip, right fiber tip, top right corner and bottom right corner of the problem domain, respectively. The center jump is the displacement jump across the surfaces of the fiber and the matrix, at the center of the fiber. The point-wise errors are computed using the L2 norm and plotted as a function of the mesh size ( $h$ ). In Figs. 8a and 8b, the fiber tip locations for all element sizes always coincide with a node. The length of the fiber is 1.44 mm, the angle of fiber is set at 68 degrees, and the left fiber tip location is at (2,1) mm from the origin (bottom left corner of mesh). The error for the corner nodes, right fiber tip and center jump reduces monotonically with increasing mesh density. Errors at the left fiber tips did not show convergence as a function of mesh density. The lack of improvement in the accuracy at point A, is attributed to much smaller absolute magnitude of deformation at point A compared to the other mesh points (i.e., B, C, D) and truncation. The error for the corner nodes, right fiber tip and center jump remained within very reasonable accuracy (i.e., less than 0.5% at the densest mesh).

The effect of fiber tip location on the accuracy characteristics of the proposed model is further investigated. Figures 8c and 8d illustrate the accuracy characteristics of the XFEM model when the fiber tips lay within the elements, at peak cohesive tractions and at the point of full separation, respectively. In these simulations, the length of the fiber is set to 2.5 mm, the angle of fiber as 45 degrees, and the left fiber tip location is positioned at (1.61, 1.62) mm from the origin. Figures 8e and 8f illustrate the accuracy characteristics of the XFEM model when the fiber tips lay on element edges. In these cases, the length of the fiber is 1.08 mm, the angle of fiber is set at 17 degrees, and the left fiber tip location is at (1.5, 3.1) mm from the origin. The XFEM model displays reasonable accuracy and follows the same monotonic trends at the corner nodes, right fiber tip and center jump irrespective of the positioning of the fibers within the matrix.

Figure 9 displays the displacement jump along the length of the fiber. At peak cohesive tractions (Figs. 9a, 9c, 9e) and at the point of full separation (Figs. 9b, 9d, 9f), respectively. Figures 9a and 9b, correspond to the case when the fiber tip locations for all element sizes

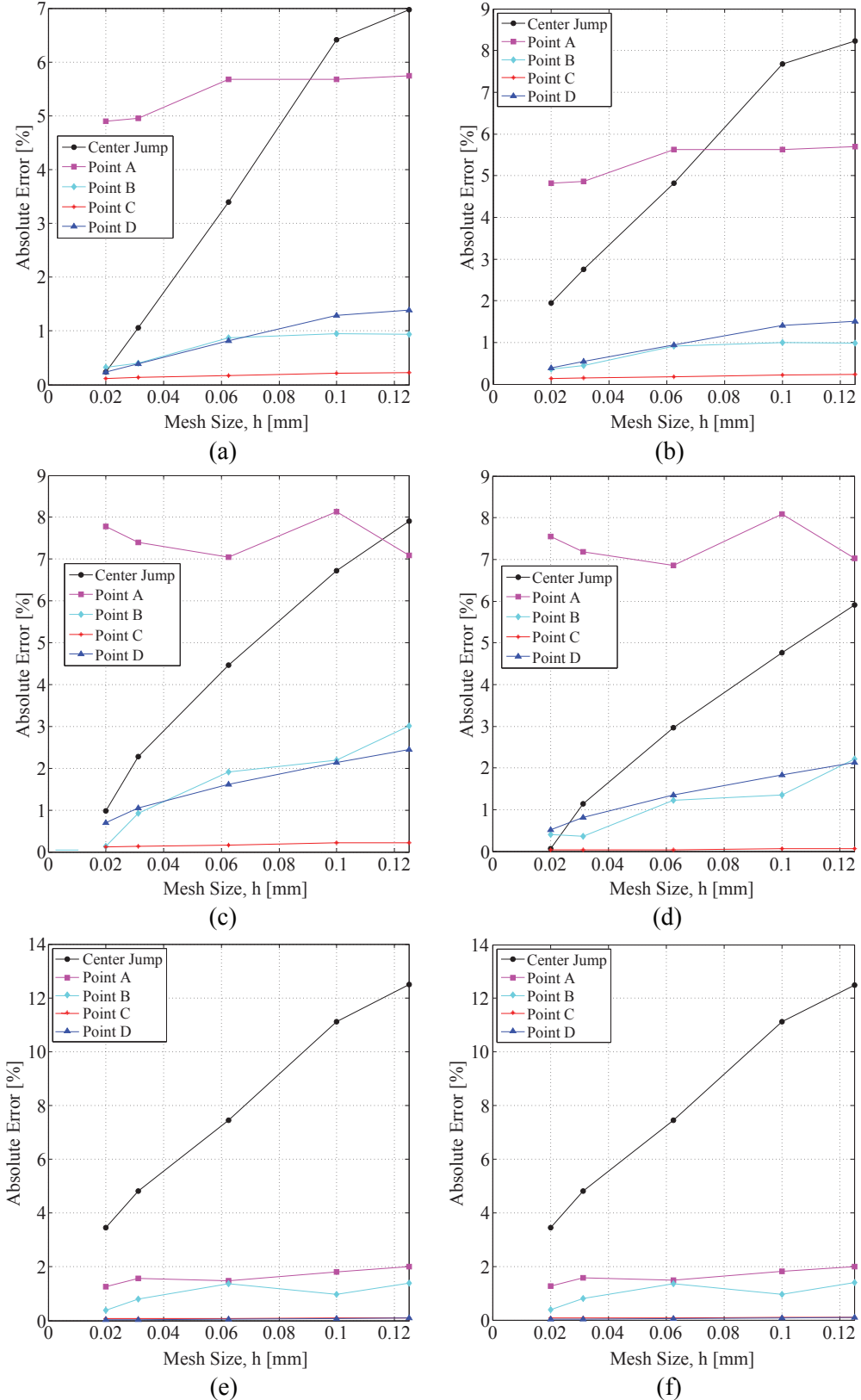


Figure 8: Point-wise error as function of mesh density. Fiber tips on element nodes ( $\theta = 68^\circ$ ): (a) peak traction and (b) post separation; fiber tips in the elements ( $\theta = 45^\circ$ ): (c) peak traction and (d) post separation; fiber tips on edges of elements ( $\theta = 17^\circ$ ): (e) peak traction and (f) post separation.

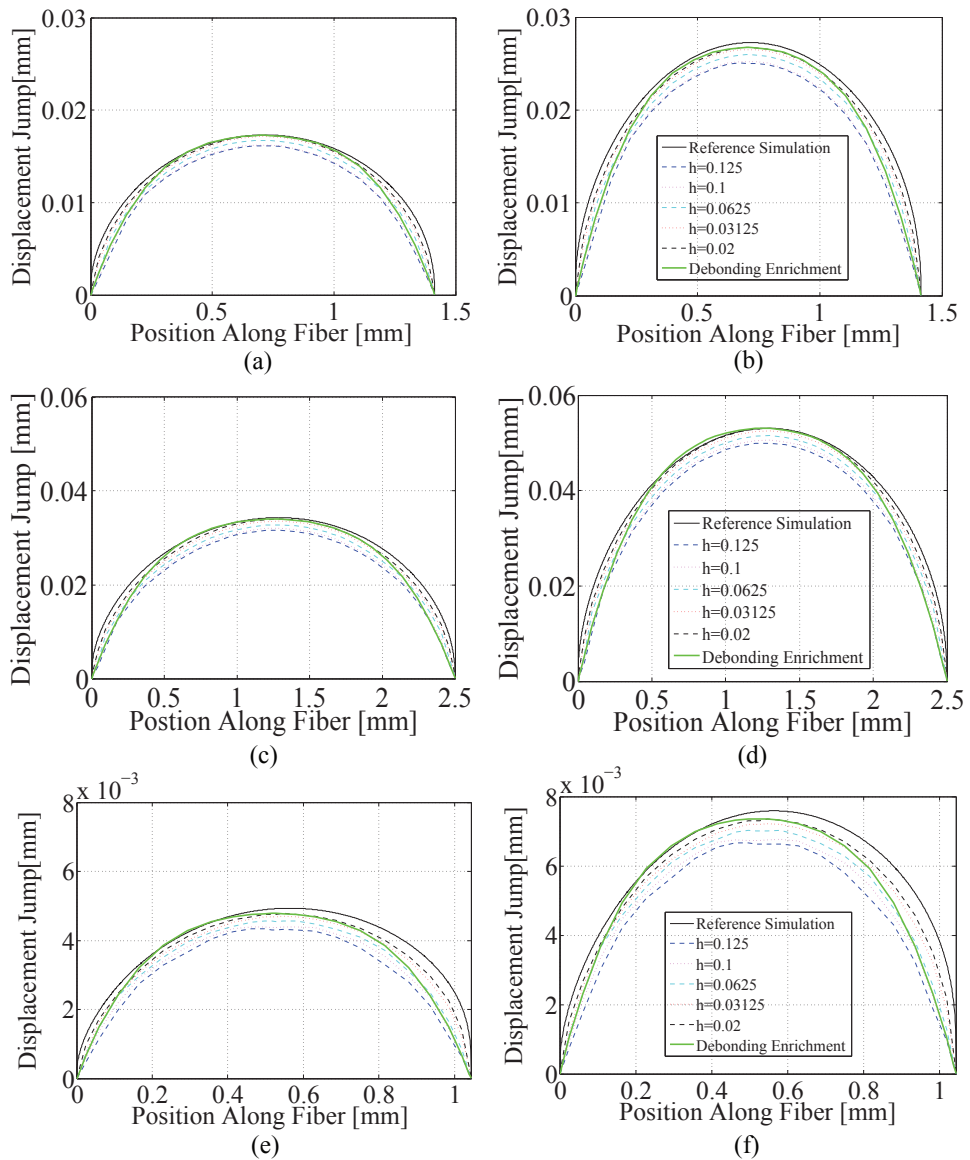


Figure 9: Displacement jump across the interface along the fiber length ( $h$  is the mesh size). Fiber tips on element nodes: (a) peak traction and (b) post separation; fiber tips in the elements: (c) peak traction and (d) post separation; fiber tips on edges of elements: (e) peak traction and (f) post separation.

always coincide with a node. The proposed model displays monotonic convergence to the reference simulations in terms of magnitude and shape of the displacement jump. Figures 9c and 9d show the variation of the displacement jump along the length of the fiber when fiber tips are positioned within elements, whereas Figs. 9e and 9f correspond to the case when the fiber tips lay on element edges, respectively. A clear convergence is observed as a function of the mesh density regardless of fiber positioning within the domain. The parabolic debonding enrichment function is plotted for the smallest mesh size ( $h=0.02\text{mm}$ ) for comparison in Fig. 9. The simulation results summarized in Fig. 9 shows a slight asymmetry in the variation of the displacement jump along the length of the fiber. The deviation from symmetry as measured from the center of the fiber is less than 5% in all cases. The slight deviation is attributed to the non-uniform stress along the length of the fiber, formed due the random positioning of the fiber. The slight variation in errors observed in Figs. 8 and 9, as a function of fiber positioning, is attributed to the accuracy of the numerical integration. In cases where the fiber tip is too close to a node, the sub elements formed in the Delaunay triangulation for numerical integration of the fully and partially enriched elements have very high aspect ratios. Nevertheless the accuracy of the proposed model is in reasonable agreement with the reference finite element model in all cases considered.

### 5.3 Two fiber case

In this section, the proposed model is verified by considering the response of a two fiber composite in the presence of matrix cracking and interface debonding at fiber-matrix interfaces. The model domain is taken as a 5 mm by 5 mm, reinforced with two fibers approximately 1 mm and 1.5 mm in length. The domain is subjected to a uniform uniaxial displacement controlled tensile loading applied at the right edge.

The matrix and fiber properties are the same as in Section 5.2. A bi-linear cohesive zone law defined by Eq. 32 and Eq. 33 is used in both the XFEM model and the reference simulation. The cohesive zone law parameters for this example are based on work from Nicholas et al. [65]. The peak normal traction and normal cohesive characteristic separation length are set as 10 MPa and 1 nm respectively. The peak shear traction and shear cohesive characteristic separation lengths are set to the same as their normal counterparts. The maximum cohesive separation length is taken as 8 nm both for normal and shear directions. The nonlocal damage model described by Eqs. 22-27 is used for both the XFEM and the reference simulations. The characteristic length of 0.07 mm and parameters  $a$  and  $b$  of 49,000 and 19.5, respectively, were employed. A mesh localization analysis is performed using three different mesh sizes identified as coarse, intermediate and fine. The coarse, intermediate and fine reference models include approximately 31,500, 120,000, and 220,000 elements, respectively. The corresponding XFEM models consist of 6,400, 25,600, and 62,500 elements, respectively. In the XFEM models, 266,

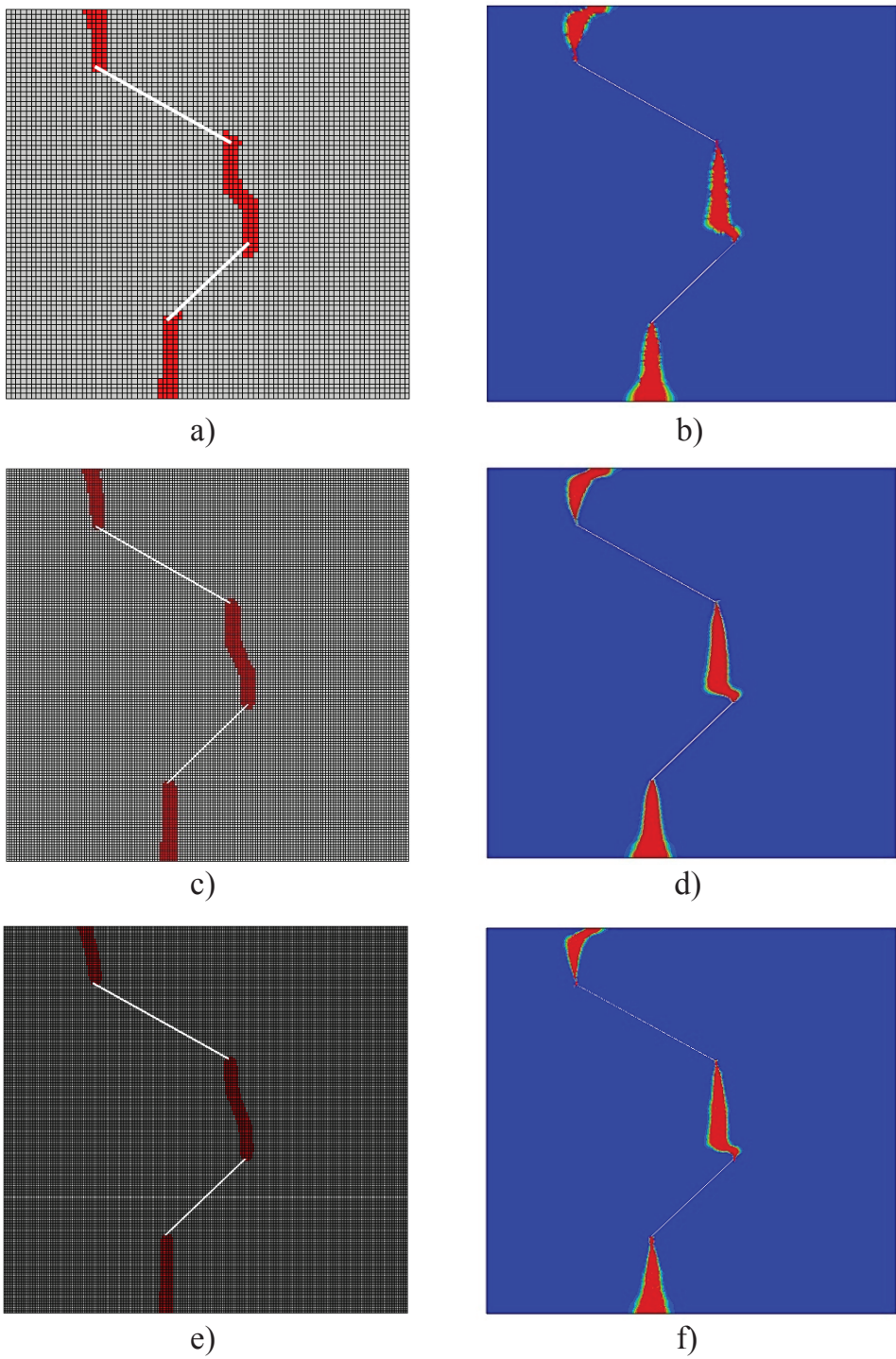


Figure 10: Damage paths of two fiber case with a nonlocal damage model. a) XFEM coarse mesh; b) reference simulation coarse mesh; c) XFEM intermediate mesh; d) reference simulation intermediate mesh; e) XFEM fine mesh; f) reference simulation fine mesh.

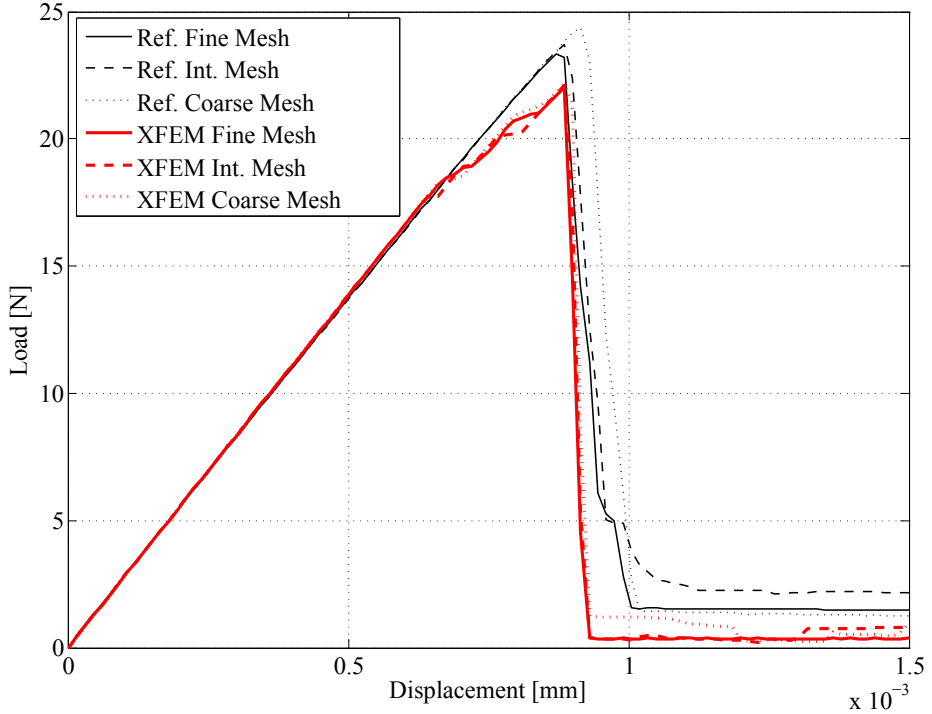


Figure 11: Load-displacement curves for XFEM and reference simulations of a two fiber case with different mesh sizes.

504, and 749 elements within the meshes are either enriched or partially enriched for the coarse, intermediate and fine cases, respectively.

Figure 10 shows the damage paths computed using the XFEM and reference simulations for the three discretizations with increasing resolution. In this example, the fiber-matrix interfaces have progressive debonding, but complete debonding does not occur. The darker (red) areas indicate that the element is fully damaged and the thin white line displays the initial fiber positions. Damage progressively extends from the left fiber tips to the top and bottom edges of the domain for the top and bottom fibers, respectively. Damage also progressively propagates between the right tips of the top and bottom fibers to create a continuous damage path between the two fibers. Both the reference and XFEM simulations display very similar thickness and location of the damage paths consistent with their specified characteristic length. The damage paths are slightly refined as the mesh density increases in both simulations, but are convergent.

The nonlocal damage paths generated using the reference finite element simulation employ a significantly larger time step size (reference simulations time step size is an order of magnitude larger than XFEM) since the computational cost of the reference simulations is very high. This leads to a slight deviation of uniformity suggested by the nonlocal integral in Eq. 27. In contrast, the damage paths generated using the XFEM approach has a uniform thickness.

The load displacement curves for the two fiber simulations computed using the XFEM and

reference simulations are displayed in Figure 11. For both the reference and XFEM simulations, the peak load and the stress-strain relationship are convergent as a function of mesh density. The proposed model displayed a slightly more progressive failure pattern that indicates at approximately 17 N. The absolute error between the respective load peaks of the XFEM and reference simulations is less than 5%. The discrepancy between the converged XFEM and reference simulation results stem from the approximations made in the kinematics of the fiber deformation as well as the fiber-matrix debonding process. The finite element analysis that is considered to be the reference solution resolves the fibers with 2-D finite elements, whereas zero measure inclusions approximate their response in the XFEM approach. The difference between the converged peak loads as well as the post peak response is primarily due to model approximations made in the current approach.

## 5.4 Random short fiber composites

The effect of interfacial properties on the performance of random short fiber reinforced composites is numerically investigated with the proposed XFEM model. A 100 mm x 100 mm domain with randomly oriented short fibers at 0.025% weight fraction is considered. The length of the fibers is also random with the mean length and standard deviation of 5 mm and 2 mm, respectively. The fibers are positioned such that no element within the domain is enriched by more than a single fiber. The domain was subjected to displacement controlled tensile loading at the right edge. Symmetry boundary conditions are imposed on the left and bottom edges. The elastic parameters of the fiber and matrix are taken to be identical to those discussed in Section 5.2. The nonlocal damage parameters of  $a=49,000$ ,  $b=19.5$  and  $l_c=1$  mm are employed to describe the failure progression within the matrix phrase.

The effect of interface properties on the failure response is investigated based on four cases. The first case is when the fibers are considered to be perfectly bonded to the matrix. In this case, the failure initiates and propagates within the matrix phase without interface interactions. The second case consists of the state of complete separation between the fibers and the matrix. All fibers are considered to be fully debonded from the matrix prior to loading at one side of the fiber as described in Section 3. The next two cases consider progressive debonding, idealized using the exponential traction-separation relationships detailed in Eq. 30 and Eq. 31. The peak traction, characteristic separation length and maximum separation length for the third case are 10 MPa, 1.2 nm, and 6 nm, respectively. The corresponding parameters for the forth case are 8 MPa, 0.01591 mm, and 0.08 mm for the normal components and 1.8 MPa, 0.01141 mm, and 0.08 mm in the tangential components, respectively.

Figure 12 shows the damage contours within the composite domain as a function of interface properties. The contours show the damage state at the end of the loading, where all cases resulted in complete loss of strength of the composite. The path of the final crack is clearly

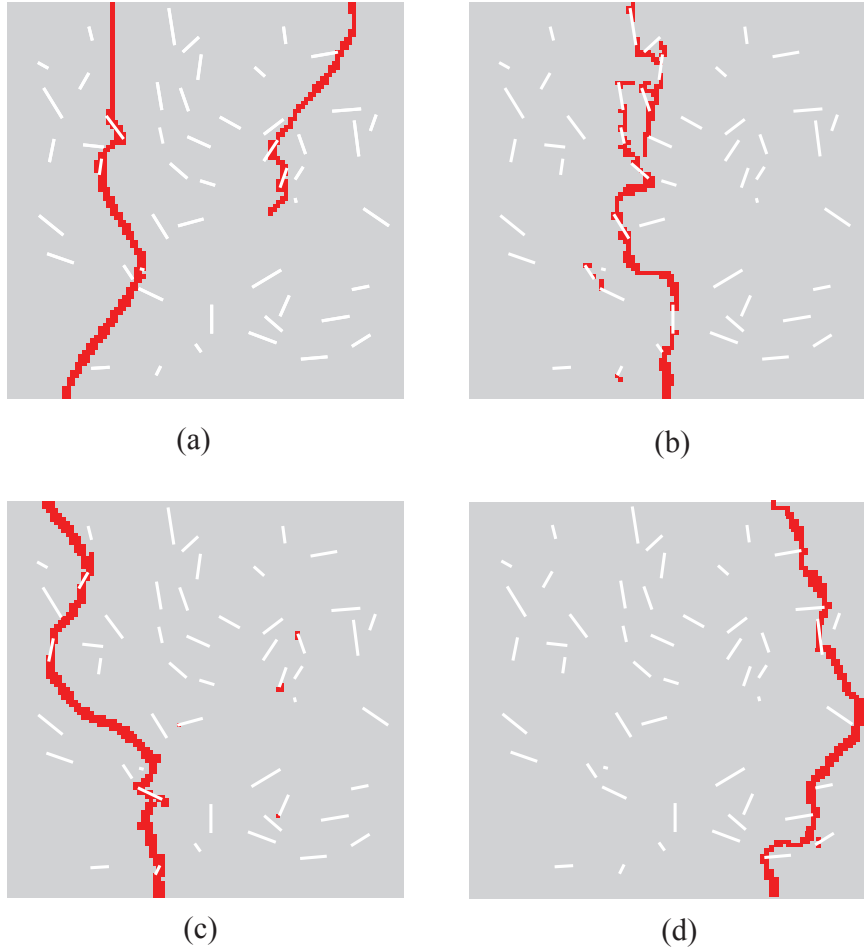


Figure 12: Damage prediction for random short fiber composites: (a) Case 1: no debonding; (b) Case 2: full debonding at the outset; (c) Case 3: weak cohesive interface; and (d) Case 4: strong cohesive interface.

significantly affected by the properties of the interfaces and is different for each of the four simulated cases. In the case of full debonding at the outset, the crack path follows the region of the highest fiber densities since the fiber locations act as pre-cracks in the absence of interface cohesion. Figure 13 shows the load-displacement curves of the composite for the four cases investigated. The strength is significantly affected by the interface characteristics. The composite strengths are 4.36 MPa, 1.95 MPa, 3.41 MPa, and 4.08 MPa for cases 1 through 4, respectively. While the strength of the composite is expected in the case of the perfect bonding, the two cases for progressive debonding show significant reduction in strength (22% and 6% for cases 3 and 4, respectively). These results point to the possible gain in composite strength if near optimal interface strength, could be achieved within the constituents. Figure 13 also demonstrates a slight reduction in composite ductility as a function of interface strength. This

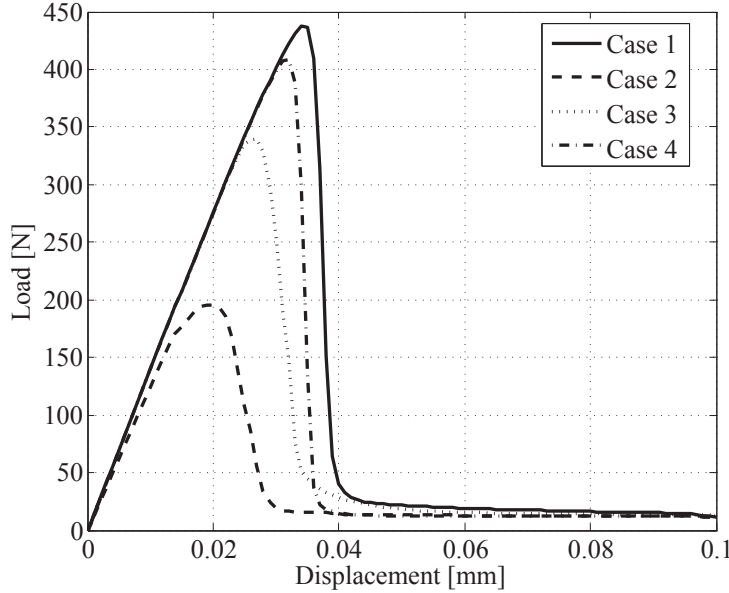


Figure 13: Load-displacement curves for the 4 cases of interface properties considered.

Fiber(s) in Domain	1	2	4	8	16	50	300
Condition Number Ratio	1.000	1.002	1.010	1.011	1.015	1.231	3.737

Table 1: Condition number ratio of the elastic stiffness matrix as a function of number of fibers in the domain.

behavior was also experimentally observed by Yoo et al. [2].

Table 1 compares the relative condition numbers of the elastic stiffness matrices of the proposed model as a function of the number of fiber enrichments. The enrichment functions slightly degrade the conditioning of the linear system but the degradation is mild, which points to the stability of the model for high weight fraction composites.

## 6 Conclusions

The formulation and implementation of XFEM modeling of progressive failure for random short fiber reinforced composites with material cohesive interfaces was proposed. The fiber inclusions were modeled as elastic objects of zero measure using the XFEM approach. A new debonding enrichment function was developed to idealize the progressive debonding between the fiber-matrix interfaces with the XFEM framework, to eliminate the need of using finite element meshes compliant with fiber inclusions. With the extension to 3-D in mind, an integral-type nonlocal damage model was used to describe the progressive cracking in the matrix. Numerical integration procedures were provided for accurate evaluation of the system response for fibers at random positions within the problem domain. The performance of

the XFEM model numerical was assessed against the direct finite element method for various fiber configurations in two dimensions. The proposed approach accurately characterizes the response of short fiber reinforced composites without the need for mesh compliance.

Several important advancements to the proposed model are under development. First, this manuscript provided the implementation details for two-dimensional problems only and the formulation is therefore applicable to short fiber composites randomly distributed along a plane but aligned along the transverse direction (two-dimensional short fiber composites). While the proposed formulation can be extended to three dimensions without conceptual difficulty, significant challenges are present in the computational implementation of the method in three-dimensions. Second is to characterize the debonding process with the use of molecular dynamics. Our near term research efforts will focus on extending the proposed modeling approach to three-dimensions and to possibly characterize the progressive debonding at the molecular level.

## Acknowledgments

The authors gratefully acknowledge the financial support from Vanderbilt University through the Discovery grant program, Vanderbilt Institute of Software Integrated Systems, and National Science Foundation CMMI division (Grant No:#0547024).

## References

- [1] J. Won, B. Hong, T. Choi, S. Lee, and J. Kang. Flexural behaviour of amorphous micro-steel fibre-reinforced cement composites. *Comp. Struct.*, 94:1443–1449, 2012.
- [2] D. Yoo, J. Lee, and Y. Yoon. Effect of fiber content on mechanical and fracture properties of ultra high performance fiber reinforced cementitious composites. *Comp. Struct.*, 106: 742–753, 2013.
- [3] V.C. Li. On engineered cementitious composites (ECC) - a review of the material and its applications. *J. of Advanced Concrete Technol.*, 1(3):215–230, 2003.
- [4] D.D.L. Chung. Cement reinforced with short carbon fibers: a multifunctional material. *Composites Part B: Engineering*, 31(6-7):511–526, 2000.
- [5] D.D.L. Chung. Composites get smart. *Materials Today*, 5(1):30–35, 2002.
- [6] F. Reza, J. A. Yamamuro, and G. B. Batson. Electrical resistance change in compact tension specimens of carbon fiber cement composites. *Cement and Concrete Compos.*, 26(7):873–881, 2004.

- [7] X. Fu and D. D. L. Chung. Submicron carbon filament cement-matrix composites for electromagnetic interference shielding. *Cement and Concrete Research*, 26(10):1467–1472, 1996.
- [8] G. P. Tandon and G. J. Weng. Average stress in the matrix and effective moduli of randomly oriented composites. *Compos. Sci. Technol.*, 27:111–132, 1986.
- [9] J. H. Huang. Some closed-form solutions for effective moduli of composites containing randomly oriented short fibers. *Mater. Sci. Engng. A*, 315:11–20, 2001.
- [10] A. Bouaziz, M. Nait-Abdelaziz, J. M. Gloaguen, and J. M. Lefebvre. Micromechanical modelling and experimental investigation of random discontinuous glass fiber polymer–matrix composites. *Compos. Sci. Technol.*, 67:3278–3285, 2007.
- [11] P. Ponte-Castaneda and J. R. Willis. The effect of spatial distribution on the effective behavior of composite materials and cracked media. *J. Mech. Phys. Solids*, 43:1919–1951, 1995.
- [12] H. J. Bohm, A. Eckschlager, and W. Han. Multi-inclusion unit cell models for metal matrix composites with randomly oriented discontinuous reinforcements. *Comp. Mater. Sci.*, 25:42–53, 2002.
- [13] H. R. Lusti, P. J. Hine, and A. A. Gusev. Direct numerical predictions for the elastic and thermoelastic properties of short fibre composites. *Compos. Sci. Technol.*, 62:1927–1934, 2002.
- [14] R. D. Crouch, S. B. Clay, and C. Oskay. Experimental and computational investigation of progressive damage accumulation in CFRP composites. *Compos. Part B: Engng.*, 48: 59.–67, 2013.
- [15] N. Moës, J. Dolbow, and T. Belytschko. A finite element method for crack growth without remeshing. *Int. J. Numer. Meth. Engng.*, 46:131–150, 1999.
- [16] T. Belytschko and T. Black. Elastic crack growth in finite elements with mimal remeshing. *Int. J. Numer. Meth. Engng.*, 45:601–620, 1999.
- [17] I. Babuska and J. M. Melenk. The partition of unity method. *Int. J. Numer. Meth. Engng.*, 40:727–758, 1997.
- [18] L. Bouhala, Q. shao, Y. Koutsawa, A. Younes, P. Nunez, A. Makradi, and S. Belouettar. An XFEM crack-tip enrichment for a crack terminating at a bi-material interface. *Engng. Fract. Mech.*, 102:51–64, 2013.

- [19] A. Legay, H. W. Wang, and T. Belytschko. Strong and weak arbitrary discontinuities in spectral finite elements. *Int. J. Numer. Meth. Engng.*, 64:991–1008, 2005.
- [20] N. Sukumar, N. Moes, B. Moran, and T. Belytschko. Extended finite element method for three-dimensional crack modelling. *Int. J. Numer. Meth. Engng.*, 48:1549–1570, 2000.
- [21] N. Sukumar and J-H. Prevost. Modeling quasi-static crack growth with the extended finite element method part 1: Computer implementation. *Int. J. Solids and Struct.*, 40: 7513–7537, 2003.
- [22] M. Lan, H. Waisman, and I. Harari. A high-order extended finite element method for extraction of mixed-mode strain energy release rates in arbitrary crack settings based on Irwins integral. *Int. J. Numer. Meth. Engng.*, 96:787–812, 2013.
- [23] B. Benowitz and H. Waisman. A spline-based enrichment function for arbitrary inclusions in extended finite element method with applications to finite deformations. *Int. J. Numer. Meth. Engng.*, 956:361–386, 2013.
- [24] J. Doblow, S. Mosso, J. Robbins, and T. Voth. Coupling volume-of-fluid based interface reconstructions with the extended finite element method. *Comp. Methods Appl. Mech. Engng.*, 197:439–447, 2008.
- [25] J. Pan and C. K. Y. Leung. Debonding along the FRP - concrete interface under combined pulling/peeling effects. *Engng. Fract. Mech.*, 74:132–150, 2007.
- [26] Y. T. Obaidat, S. Heyden, and O.Dahlblom. The effect of CFRP and CFRP/concrete interface models when modelling retrofitted RC beams with FEM. *Comp. Struct.*, 92: 1391–1398, 2010.
- [27] I.G. Garcia, M. Paggi, and V. Mantic. Fiber-size effects on the onset of fiber-matrix debonding under transverse tension: A comparison between cohesive zone and finite fracture mechanics models. *Engng. Fract. Mech.*, 115:96–110, 2014.
- [28] J. Wang. Cohesive zone model of frp-concrete interface debonding under mixed-mode loading. *Int. J. of Solids and Struct.*, 44:6551–6568, 2007.
- [29] S. Li, M.D. Thouless, A.M. Waas, J.A. Schroeder, and P.D. Zavattieri. Mixed-mode cohesive-zone models for fracture of an adhesively bonded polymermatrix composite. *Engng. Fract. Mech.*, 73:64–78, 2006.

- [30] C. Oskay and J. Fish. Eigendeformation-based reduced order homogenization for failure analysis of heterogeneous materials. *Comput. Methods Appl. Mech. Engrg.*, 196:1216–1243, 2007.
- [31] H. Yan, C. Oskay, A. Krishnan, and L. R. Xu. Compression-after-impact response of woven fiber-reinforced composites. *Compos. Sci. Technol.*, 70:2128–2136, 2010.
- [32] N. Moës and T. Belytschko. Extended finite element method for cohesive crack growth. *Engng. Fract. Mech.*, 69:813–833, 2002.
- [33] J. Unger, S. Eckardt, and C. Konke. Modelling of cohesive crack growth in concrete structures with the extended finite element method. *Comput. Methods Appl. Mech. Engng.*, 196:4087–4100, 2007.
- [34] G. Zi and T. Belytschko. New crack-tip elements for XFEM and applications to cohesive cracks. *Int. J. Numer. Meth. Engng.*, 57:2221–2240, 2003.
- [35] J.L. Asfreg, P.N. Poulsen, and L.O. Nielsen. A consistent partly cracked XFEM element for cohesive crack growth. *Int. J. Numer. Meth. Engng.*, 72:464–485, 2007.
- [36] L. Bouhala, A. Makradi, S. Belouettar, H. Kiefer-Kamal, and P. Freres. Modelling of failure in long fibres reinforced composites by X-FEM and cohesive zone model. *Composites: Part B*, 55:353–361, 2013.
- [37] E. Benvenuti. A regularized XFEM framework for embedded cohesive interfaces. *Comput. Methods Appl. Mech. Engng.*, 197:4367–4378, 2008.
- [38] T. Hettich and E. Ramm. Modeling of failure in composites by X-FEM and level sets within a multiscale framework. *Comput. Methods Appl. Mech. Engng.*, 197:414–424, 2008.
- [39] F.K.F. Radtke, A. Simone, and L.J. Sluys. A partition of unity finite element method for obtaining elastic properties of continua with embedded thin fibres. *Int. J. Numer. Meth. Engng.*, 84:708–732, 2010.
- [40] F.K.F. Radtke, A. Simone, and L.J. Sluys. A partition of unity finite element method for simulating non-linear debonding and matrix failure in thin fibre composites. *Int. J. Numer. Meth. Engng.*, 86:453–476, 2011.
- [41] M. Pike and C. Oskay. Modeling random short nanofiber- and microfiber-reinforced composites using the extended finite-element method. *J. Nanomech. Micromech.*, 2014.

- [42] N. Moës, M. Cloirec, P. Cartraud, and J.-F. Remacle. A computational approach to handle complex microstructure geometries. *Comput. Methods Appl. Mech. Engng.*, 192: 3163–3177, 2003.
- [43] G. Ventura, E. Budyn, and T. Belytschko. Vector level sets for description of propagating cracks in finite elements. *Int. J. Numer. Meth. Engng.*, 58:1571–1592, 2003.
- [44] N. Sukumar, D.L. Chopp, and B. Moran. Extended finite element method and fast marching method for three-dimensional fatigue crack propagation. *Engng. Fract. Mech.*, 70:29–48, 2003.
- [45] C. Richardson, J. Hegemann, E. Sifakis, J. Hellrung, and J. Teran. An XFEM method for modeling geometrically elaborate crack propagation in brittle materials. *Int. J. Numer. Meth. Engng.*, 88:1042–1065, 2011.
- [46] M. Jirasek. Nonlocal models for damage and fracture: comparison of approaches. *Int. J. of Solids and Struct.*, 35:4133–4145, 1998.
- [47] M. Jirasek. Non-local damage mechanics with application to concrete. *Revue Franaise de Gnie Civil*, 8:683–707, 2004.
- [48] Z. Bazant and M. Jirasek. Nonlocal integral formulations of plasticity and damage: Survey of progress. *J. of Engng. Mech.*, 128:1119– 1149, 2002.
- [49] M. G. D. Geers, W. A. M. Brekelmans, and R. de Borst. Viscous regularization of strain-localisation for damaging materials. In *DIANA Computational Mechanics*. Springer Netherlands, 1994.
- [50] G. Thiagarajan, K. Hsia, and Y. Huang. Finite element implementation of virtual internal bond model for simulating crack behavior. *Engng. Fract. Mech.*, 71:401–432, 2004.
- [51] K. Garikipati and T.J.R. Hughes. A variational multiscale approach to strain localization formulation for multidimensional problem. *Comp. Methods Appl. Mech. Engng.*, 188: 39–60, 2000.
- [52] J. Fish and C. Oskay. A nonlocal multiscale fatigue model. *Mech. of Adv. Mat. and Struct.*, 12:485–500, 2005.
- [53] M. di Prisco and J. Mazars. "Crush-crack": a non -local damage model for concrete. *Mech. of Cohesive-Frictional Mater.*, 1:312–347, 1996.
- [54] H. Wendland. Piecewise polynomial, positive definite and compactly supported radial functions of minimal degree. *Advances in Comp. Math.*, 4:389–396, 1995.

- [55] X.-P. Xu and A. Needleman. Numerical simulations of fast crack growth in brittle solids. *J. Mech. Phys. Solids*, 42:1397–1434, 1994.
- [56] X.-P. Xu and A. Needleman. Void nucleation by inclusion debonding in a crystal matrix. *Modelling Simul. Mater. Sci. Engng.*, 1:111–132, 1993.
- [57] A. Aimi and M. Diligenti an F. Freddi. Numerical aspects in the SGBEM solution of softening cohesive interface problems. *J. of Comp. and Appl. Math.*, 210:22–33, 2007.
- [58] A. Carpinteri. Softening and snap-back instability in cohesive solids. *Int. J. Numer. Meth. Engng.*, 28:1521–1537, 1989.
- [59] L. Chen, T. Rabczuk, S. P. A. Bordas, G. R. Liu, K. Y. Zeng, and P. Kerfriden. Extended finite element method with edge-based strain smoothing (ESm-XFEM) for linear elastic crack growth. *Comput. Methods Appl. Mech. Engng.*, 209:250–265, 2012.
- [60] T.P. Fries. A corrected XFEM approximation without problems in blending elements. *Int. J. Numer. Meth. Engng.*, 75:503–532, 2008.
- [61] J. Chessa, H. Wang, and T.Belytschko. On the construction of blending elements for local partition of unity enriched finite elements. *Int. J. Numer. Meth. Engng.*, 57:1015–1038, 2003.
- [62] P. Laborde, J. Pommier, Y. Renard, and M. Salaun. High-order extended finite element method for cracked domains. *Int. J. Numer. Meth. Engng.*, 64:354–381, 2005.
- [63] N. Pan. The elastic constants of randomly oriented fiber composites: A new approach to prediction. *Science and Engrg. of Composite Materials*, 5:63–72, 1996.
- [64] J. Wang. Cohesive zone model of intermediate crack-induced debonding of FRP-plated concrete beam. *Int. J. Solids and Struct.*, 43:6630–6648, 2006.
- [65] T. Nicholas, D. Boyajian, S.E. Chen, and A. Zhou. Finite element modeling of mode I failure of the single contoured cantilever CFRP-reinforced concrete beam. *J. of Struct.*, 2013:1–8, 2013.